

# An energy charge sensor for balancing RNA polymerase recycling and hibernation

Markus Wahl (✉ [mwahl@zedat.fu-berlin.de](mailto:mwahl@zedat.fu-berlin.de))

Freie Universität Berlin <https://orcid.org/0000-0002-2811-5307>

Hao-Hong Pei

Freie Universität Berlin

Tarek Hilal

Freie Universität Berlin

Zhuo Chen

Technische Universität Berlin

Yong-Heng Huang

Freie Universität Berlin

Yuan Gao

Freie Universität Berlin

Nelly Said

Freie Universität Berlin

Bernhard Loll

Freie Universität Berlin <https://orcid.org/0000-0001-7928-4488>

Juri Rappsilber

Technische Universität Berlin <https://orcid.org/0000-0001-5999-1310>

Georgiy Belogurov

University of Turku <https://orcid.org/0000-0002-3070-6843>

Irina Artsimovitch

The Center for RNA Biology, Ohio State University

---

## Article

**Keywords:** Cellular RNA polymerases, *Bacillus subtilis*

**Posted Date:** July 16th, 2020

**DOI:** <https://doi.org/10.21203/rs.3.rs-40617/v1>

**License:**   This work is licensed under a Creative Commons Attribution 4.0 International License.

[Read Full License](#)

**Version of Record:** A version of this preprint was published at Nature Communications on December 18th, 2020. See the published version at <https://doi.org/10.1038/s41467-020-20159-3>.

# Abstract

Cellular RNA polymerases can become trapped on DNA or RNA, threatening genome stability and limiting free enzyme pools, or enter dormancy. How RNA polymerase recycling into active states is achieved and balanced with quiescence remains elusive. We structurally analyzed *Bacillus subtilis* RNA polymerase bound to the NTPase HelD. HelD has two long arms: a Gre cleavage factor-like coiled-coil inserts deep into the RNA polymerase secondary channel, dismantling the active site and displacing RNA; a unique helical protrusion inserts into the main channel, prying  $\beta$  and  $\beta'$  subunits apart and dislodging DNA, aided by the  $\delta$  subunit. HelD release depends on ATP, and a dimeric structure resembling hibernating RNA polymerase I suggests that HelD can induce dormancy at low energy levels. Our results reveal an ingenious mechanism by which active RNA polymerase pools are adjusted in response to the nutritional state.

## Main

(RNAPs) bacterial RNAPs minimally comprise an  $\alpha_2\beta\beta'\omega$  subunit catalytic core, which forms a holoenzyme with one of several  $\sigma$  factors to initiate transcription at a promoter.<sup>1</sup> After promoter escape, elongation factors replace  $\sigma$ , and the ensuing elongation complex (EC) synthesizes RNA until a termination signal is reached. At a terminator, bacterial EC is abruptly destabilized by either an oligo-U-tailed G/C-rich RNA hairpin or by an RNA translocase/helicase  $\rho$ .<sup>2</sup> However, RNAP can linger on DNA after RNA release<sup>3-5</sup>, roadblocking replisomes to trigger double-stranded DNA breaks<sup>6</sup> and giving rise to aberrant antisense transcripts<sup>5</sup>. RNAP can also form binary complexes with RNA<sup>7,8</sup>, either through *de novo* association with stable RNAs, such as tRNAs and 6S RNA<sup>9,10</sup>, or in the course of hairpin-induced termination<sup>11</sup>. While some RNA binary complexes serve as RNAP storage depots and can be reactivated when nutrients become available<sup>10</sup>, others may sequester unproductive RNAP<sup>12</sup>.

Post-termination binary complexes have to be dismantled to recycle RNAP, and ordered recycling is considered an integral phase of the duty cycle of many molecular machines, such as ribosomes<sup>13</sup>. By contrast, recycling has so far not garnered similar attention in bacterial transcription. While several accessory proteins could facilitate RNAP detachment from nucleic acids, including  $\sigma$ <sup>8,9</sup>, transcription repair coupling factor Mfd<sup>14</sup>,  $\rho$ <sup>6</sup> and the NTPase RapA<sup>15</sup>, they release stalled RNAP under specific circumstances rather than acting as genuine recycling factors.

RNAPs from some Gram-positive bacteria, including *Bacillus subtilis*, contain additional small subunits,  $\delta$  and  $\epsilon$ .  $\delta$  influences promoter selection<sup>16</sup> and regulation by the initiating NTP<sup>17</sup> and can promote RNAP recycling<sup>16</sup> by displacing  $\sigma$  from holoenzyme<sup>18</sup> and RNA from binary complexes<sup>7</sup>. The function of  $\epsilon$  remains enigmatic<sup>19</sup>.

HelD, a putative superfamily I nucleic acid-dependent NTPase found in Gram-positive bacteria, is related to UvrD and Rep helicases of *Escherichia coli*<sup>20</sup>. HelD has been implicated in DNA repair and

recombination<sup>21</sup> and adaption to environmental changes<sup>22</sup>. *B. subtilis* HelD and RNAP directly interact<sup>22</sup> and are present at comparable levels during sporulation<sup>23</sup>. Together with  $\delta$ , HelD enhances RNAP cycling<sup>22</sup>. We hypothesized that HelD is a general recycling factor and set out to elucidate its mechanism of action.

## Results

### Structural analysis of RNAP- $\delta$ -HelD complexes

RNAP enriched from stationary phase *B. subtilis* cells exhibited an  $\alpha_2\beta\beta'\delta\epsilon\omega$  subunit composition, with sub-stoichiometric amounts of HelD, PriA,  $\sigma^A$  and  $\sigma^B$  (Extended Data Fig. 1a). RNAP variants lacking HelD (RNAP $^{\Delta\text{HelD}}$ ) or lacking  $\delta$  and HelD (RNAP $^{\Delta\delta\Delta\text{HelD}}$ ) were purified from *B. subtilis*  $\Delta\text{helD}$  and  $\Delta\text{helD}\Delta\text{rpoE}$  strains, respectively (Extended Data Table 1); RNAP $^{\Delta\text{HelD}}$  showed a marked loss of  $\omega$  (Extended Data Fig. 1b).

We assembled an RNAP- $\delta$ -HelD complex by supplementing stationary phase RNAP with  $\delta$ , HelD, and a DNA/RNA scaffold with an artificial transcription bubble (Extended Data Table 1), followed by size exclusion chromatography (SEC). RNAP bound HelD but not the nucleic acid scaffold, and  $\omega$  was again underrepresented in the RNAP- $\delta$ -HelD fractions (Extended Data Fig. 1c). Cryo-electron microscopy (cryoEM) data were collected after vitrifying purified complexes without crosslinking in the presence of detergent to overcome preferred particle orientations (Extended Data Fig. 2). For structure analysis, we iteratively extracted  $\sim 1,000,000$  particle images from  $\sim 9,100$  micrographs for multi-particle 3D refinement (Extended Data Fig. 3a). Refinement led to two maps for monomeric RNAP- $\delta$ -HelD and dimeric (RNAP- $\delta$ -HelD)<sub>2</sub> complexes at global resolutions of 4.2 Å and 3.9 Å, respectively; local resolutions in both structures extended to well below 3.0 Å (Extended Data Fig. 3b; Extended Data Table 2).

In both monomeric and dimeric complexes, we observed well-defined density for RNAP subunits  $\alpha 1/2$  (N-terminal domains [NTDs]),  $\beta$ ,  $\beta'$ ,  $\delta$ ,  $\epsilon$  and HelD (Extended Data Fig. 4). Density for the  $\omega$  subunit or nucleic acids was missing. Unless mentioned otherwise, the following descriptions refer to the monomeric complex.

### Organization of RNAP in an RNAP- $\delta$ -HelD complex

In the RNAP- $\delta$ -HelD complex, RNAP adopts a conformation in which the main channel, where downstream DNA and the RNA:DNA hybrid are accommodated in an EC, is wide open, with a distance of  $\sim 52$  Å between the  $\beta 2$  lobe (P242) and the  $\beta'$  clamp helices (N283), compared to  $\sim 18$  Å between the corresponding elements in the *E. coli* EC<sup>24</sup> (Fig. 1a,b; Extended Data Table 3; Supplementary Data 1), and a concomitant widening of the RNA exit tunnel by more than 17 Å ( $\beta$  flap<sup>R800</sup> to  $\beta'$  lid<sup>D245</sup>). Comparison to the *E. coli* EC showed that RNAP opening leads to repositioning of the  $\beta'$  secondary channel elements, which would clash with  $\omega$  at its canonical binding site, explaining loss of  $\omega$  upon assembly of the RNAP- $\delta$ -HelD complex. The  $\alpha 1/2^{\text{NTD}}$ s dimer remains bound at the closed end of the open  $\beta/\beta'$  crab claw.

The  $\epsilon$  subunit is positioned in a cavity formed by the  $\alpha 1/2$  NTDs, the C-terminal  $\beta$  clamp, and  $\beta'$  residues 492-655 that form part of the secondary channel (Fig. 1a), in contrast to previous mapping of  $\epsilon$  at the  $\beta'$  jaw based on a low-resolution cryoEM analysis and structural similarity of  $\epsilon$  to the phage T7 Gp2<sup>19</sup>. The  $\epsilon$  subunit of *B. subtilis* RNAP occupies a position analogous to a small domain in archaeal and eukaryotic nuclear RNAPs from homologs of the bacterial  $\alpha 1$  subunit (D, Rpb3 and AC40 of archaeal RNAP; eukaryotic RNAP II and eukaryotic RNAP I/III, respectively; Fig. 2). In some archaeal and eukaryotic RNAPs, these small domains bind an 4Fe-4S cluster<sup>25</sup>. *B. subtilis* RNAP, but not the *E. coli* enzyme, features a cavity that could accommodate an equivalent of the archaeal subunit N (Rpb10 in eukaryotic RNAP I, II and III), but remains unoccupied in the present structures.  $\epsilon$  may support the structural integrity of RNAP, securing interactions between  $\alpha$ ,  $\beta$  and  $\beta'$  subunits when  $\beta$  and  $\beta'$  are forced apart by HelD (see below).

The  $\delta$  subunit consists of a globular N-terminal domain (NTD; residues 1-90), and an intrinsically disordered, highly acidic C-terminal region (CTR; residues 91-173)<sup>7</sup>.  $\delta^{\text{NTD}}$  resides on the surface of RNAP between the  $\beta'$  shelf and jaw (Fig. 1a), in agreement with a previous *in vivo* crosslinking/mass spectrometry (CLMS) analysis<sup>26</sup>, and contributes to main channel opening by contracting the  $\beta'$  shelf and jaw compared to the *E. coli* EC<sup>24</sup>.

### HelD invades RNAP channels

HelD consists of four domains/regions: an N-terminal region (NTR; residues 4-187), two globular domains (D1a/D1b, residues 188-338/491-603; D2, residues 604-774), and an elongated helical protrusion in D1 (HelD<sup>Bumper</sup>; residues 339-490; Fig. 3a). The NTR exhibits remarkable resemblance to GreA/B transcript cleavage factors, but with an extended coiled-coil (HelD<sup>Pike</sup>; residues 4-96; Fig. 1c; Fig. 3b). D1 and D2 resemble NTPase/helicase domains of UvrD<sup>27</sup>, with a subdomain deleted from D2 and HelD<sup>Bumper</sup> inserted into D1 (Fig. 3c). HelD<sup>Bumper</sup> lacks close structural similarity to other proteins in the Protein Data Bank (<https://www.rcsb.org>).

HelD resembles a two-pronged fork poking into RNAP. In perfect analogy to transcript cleavage factors<sup>28</sup>, one prong, HelD<sup>Pike</sup>, inserts deeply into the secondary channel, through which substrate NTPs enter the RNAP active site during elongation (Fig. 1a,c). D1/D2 reach around the  $\beta 2$  lobe, positioning the other prong, HelD<sup>Bumper</sup>, in the main channel where it pushes against the  $\beta'$  clamp, forcing  $\beta$  and  $\beta'$  apart (Fig. 1a). In the course of HelD engaging RNAP, a large combined surface area ( $\sim 11,500 \text{ \AA}^2$ ;  $\sim 8,000 \text{ \AA}^2$  with  $\beta'$ ;  $\sim 1,800 \text{ \AA}^2$  with  $\beta$ ;  $\sim 1,700 \text{ \AA}^2$  with  $\delta$ ) is buried.

To confirm contacts and the dramatic structural rearrangements triggered by HelD binding, we used RNAP $\Delta\delta\Delta\text{HelD}$  and recombinant  $\delta$  and HelD to assemble RNAP $\Delta\delta\Delta\text{HelD}$ - $\delta$ , RNAP $\Delta\delta\Delta\text{HelD}$ -HelD and RNAP $\Delta\delta\Delta\text{HelD}$ - $\delta$ -HelD, and mapped molecular neighborhoods in these complexes and RNAP $\Delta\delta\Delta\text{HelD}$  by CLMS with the heterobifunctional, photoactivatable crosslinker sulfosuccinimidyl 4,4'-azipentanoate (sulfo-SDA; Fig. 4a,b; Extended Data Table 4; Supplementary Table 1). Matching the  $\delta^{\text{NTD}}$  binding site

deduced by cryoEM, a short stretch of  $\delta$  residues crosslinked to the  $\beta'$  jaw in both RNAP $\Delta\delta\Delta$ HeID- $\delta$  ( $\delta^{Y82,P83,Y85}-\beta'^{K1032}$ ) and RNAP $\Delta\delta\Delta$ HeID- $\delta$ -HeID ( $\delta^{Y83,Y85,L87,E90}-\beta'^{K1032}$ ). Multiple crosslinks of HeID were identified for RNAP $\Delta\delta\Delta$ HeID-HeID and RNAP $\Delta\delta\Delta$ HeID- $\delta$ -HeID complexes inside the RNAP main channel, along the region connecting the main and secondary channels, and in the active site region, in excellent agreement with our cryoEM structures (Extended Data Fig. 5). RNAP $\Delta\delta\Delta$ HeID, RNAP $\Delta\delta\Delta$ HeID- $\delta$  and RNAP $\Delta\delta\Delta$ HeID-HeID yielded many over-length crosslinks when compared to the RNAP- $\delta$ -HeID structure (Fig. 4c,d). A specific set of crosslinks between the  $\beta$ 1/2 lobes (residues 146-248) and the  $\beta'$  shelf and jaw (residues 794-1141) represents a conformation in which  $\beta$  and  $\beta'$  approach each other across the main channel unless both  $\delta$  and HeID are bound to RNAP (Fig. 4e,f). Together, our results demonstrate that HeID interacts with the main and the secondary channels of RNAP and that stable main channel opening depends on the presence of both  $\delta$  and HeID.

### HeID<sup>Pike</sup> dismantles the RNAP active site and competes with RNA

Upon penetrating the secondary channel, HeID<sup>Pike</sup> locally disrupts the  $\beta'$  bridge helix (BH; between residues 780 and 787) and locks the  $\beta'$  trigger loop (TL; Fig. 5), *i.e.* key elements that rearrange for nucleotide addition during elongation<sup>29</sup>. While HeID<sup>Pike</sup> carries negatively charged side chains (D56, D57, E60) at its tip, these residues do not remodel the active site as observed with GreB<sup>28</sup>. Instead, the tip plows through the active site, thereby dismantling it. The  $\beta$  C-terminal clamp is pushed away from the nucleic acids,  $\beta$  switch region 3 (Sw3), which lines the hybrid in the EC, becomes disordered and the active site loop (ASL) is rearranged so that the catalytic Mg<sup>2+</sup> ion is lost (Fig. 5).

RNAP-RNA binary complexes are catalytically active, implying that RNA resides in the active site cavity<sup>8</sup>. As seen by comparison with an *E. coli* EC<sup>24</sup>, the HeID<sup>Pike</sup> tip binds in direct competition to RNA in the hybrid (Fig. 6a) and may additionally repel RNA *via* the negatively charged residues. Thus, HeID<sup>Pike</sup> rearranges active site regions and spatially competes with all RNAs bound in the vicinity. RNA release is facilitated by RNA exit tunnel opening *via* HeID<sup>Bumper</sup>.

### HeID<sup>Bumper</sup> and $\delta$ pry the main channel open and displace DNA

Due to the combined actions of  $\delta$ <sup>NTD</sup> and HeID<sup>Bumper</sup>, RNAP- $\delta$ -HeID exhibits the most open main channel configuration observed in RNAP complexes to date, augmented by more than 20 Å relative to a *Mycobacterium smegmatis*  $\sigma^A$  holoenzyme<sup>30</sup> (Fig. 6b,c). We observed cryoEM density around HeID<sup>Bumper</sup> that could only be interpreted by the intrinsically disordered, acidic  $\delta$ <sup>CTR</sup>. We confirmed direct HeID- $\delta$  interaction *via*  $\delta$ <sup>CTR</sup> by analytical SEC; while HeID co-migrated with  $\delta$  and the complex eluted earlier than the individual proteins (Fig. 6d), no such interaction was detected with  $\delta$ <sup>NTD</sup> (Fig. 6e). Thus,  $\delta$ <sup>CTR</sup> supports HeID in its push against the  $\beta'$  clamp by reaching across the main channel and encircling HeID<sup>Bumper</sup> (Fig. 1a), and occupies regions next to the  $\beta$  subunit where downstream DNA is accommodated in the EC (Fig.

6b). Clearly, binding of HelD<sup>Bumper</sup> and  $\delta^{\text{CTR}}$  in the main channel is incompatible with DNA occupying this site, explaining why a nucleic acid scaffold fails to bind the RNAP- $\delta$ -HelD complex (Extended Data Fig. 1c; Supplementary Data 2).

To further delineate the contributions of  $\delta$  and HelD to DNA displacement, we conducted band shift assays. HelD displaced about 20 % of DNA from RNAP <sup>$\Delta\delta\Delta$ HelD</sup>, while  $\delta$  led to about 80 % displacement in the absence of HelD (Fig. 6f, lanes 4-6). This finding is consistent with the observation that  $\delta^{\text{CTR}}$  alone can displace RNA or DNA from RNAP, albeit only if present in large excess<sup>7</sup>. Increasing amounts of  $\delta$  titrated to DNA-bound RNAP <sup>$\Delta\delta\Delta$ HelD</sup> in the presence of HelD led to gradual reduction of bound DNA, with essentially all DNA displaced when equimolar amounts of  $\delta$  relative to RNAP <sup>$\Delta\delta\Delta$ HelD</sup>-HelD were added (Fig. 6f, lanes 7-13). Under otherwise identical conditions only ~50 % of the DNA were displaced by addition of  $\delta^{\text{NTD}}$  (Fig. 6f, lane 14). Together, these results underscore the importance of  $\delta$  in DNA displacement, show that HelD is required to achieve complete DNA release, and support the cooperation of  $\delta^{\text{CTR}}$  and HelD inferred from our structure and CLMS.

Notably, HelD/ $\delta$ -mediated DNA displacement did not require ATP. Furthermore, comparison with DNA-bound UvrD<sup>27</sup> revealed that the template strand would be continuous with a putative HelD-loaded strand, and that conformational changes would be required for HelD to accommodate a DNA strand at D1/D2 in a UvrD-like manner (Fig. 4d). However, as DNA displacement is supported by transcription bubble rewinding<sup>31</sup>, it is unlikely that HelD captures single-stranded DNA at the position revealed in our structure. Our analysis, therefore, indicates that neither DNA binding nor unwinding by HelD is required for RNAP recycling, consistent with lack of helicase activity in isolated HelD<sup>22</sup>.

### ATP-dependent HelD release

As HelD completely incapacitates RNAP (Fig. 5a,b), it has to be released to allow transcription to resume.  $\sigma^A$  did not displace HelD in SEC (Expanded Data Fig. 6a). Comparison of UvrD bound to DNA and ADP-Mg<sub>2</sub>F<sub>3</sub><sup>27</sup> showed that the D1/D2 conformation of RNAP-bound HelD is incompatible with ATP binding (Fig. 7a). We thus surmised that ATP-bound HelD may have a lower affinity for RNAP than the apo factor. Consistent with this notion, ATP $\gamma$ S, AMPPNP and, to a somewhat lesser extent, ATP led to release of HelD from RNAP- $\delta$ -HelD during SEC, while ADP or AMP had minor effects (Fig. 7b; Extended Data Fig. 6b). AMPPNP and ATP $\gamma$ S mimic conditions of constantly high ATP supply, whereas ATP is likely hydrolyzed and separated from RNAP/HelD during SEC, reducing its effect. Although ATP and analogs lead to HelD release, ATP-bound HelD most likely retains physiologically relevant affinity for RNAP, as evident from its ATP-dependent stimulatory effect on transcription<sup>22</sup>.

### Dimeric RNAP- $\delta$ -HelD

About two thirds of our particle images conformed to dimeric (RNAP- $\delta$ -HelD)<sub>2</sub> complexes (Fig. 7c; Supplementary Data 3), which were not sufficiently stable during SEC (Extended Data Fig. 1d). The protomers of the dimeric assembly closely resemble the monomeric RNAP- $\delta$ -HelD complex (root-mean-

square deviation of 1.2-1.3 Å for 23,360-23,971 pairs of Ca atoms), but elements of the RNAP active site are further remodeled in the dimer (Fig. 5a,b). The HelD-repositioned clamp forms an essential contact region in the dimer, which also sequesters the initiation/elongation factor-binding  $\beta$  flap tip (FT; Fig. 7c). The dimeric RNAP- $\delta$ -HelD complex shows striking resemblance to the hibernating dimeric eukaryotic RNAP I<sup>32-34</sup>, with analogous regions contributing to the dimer interfaces (Fig. 7d). These observations suggest that, like the RNAP I dimer, dimeric RNAP- $\delta$ -HelD represents a dormant state.

## Discussion

Results of this and the accompanying reports (Newing *et al.*, submitted; Kuba *et al.*, submitted) show that HelD mounts a two-pronged attack at the RNAP main and secondary channels. Both *B. subtilis* and distantly related *M. smegmatis* HelD pinch RNAP around the BH, widen the main and RNA exit channels to provide escape routes for DNA and RNA, and displace the bound nucleic acids. However, the exact implementations of this conserved mechanism are distinct. *B. subtilis* HelD uses similarly sized arms to penetrate deeply into the channels, with  $\delta$  playing a supporting role.  $\delta^{\text{NTD}}$  aids the main channel opening, whereas  $\delta^{\text{CTR}}$  may support HelD recruitment and guide HelD<sup>Bumper</sup> into the main channel to avoid topological trapping of DNA. In contrast, *M. smegmatis* HelD has evolved a branched main channel arm that functionally compensates for the absence of  $\delta$  and for a rudimentary secondary channel arm, which merely helps HelD anchoring on RNAP. We presume that the large surface area buried upon RNAP-HelD complex formation, rather than HelD ATPase, provides the driving force for the dramatic RNAP opening.

To engage RNAP, HelD reaches around the  $\beta 2$  lobe, a mode of attack that is not possible with RNAPs containing a  $\beta'$  lineage-specific insertion, SI3, stacked onto the  $\beta 2$  lobe, such as *E. coli* (Extended Data Fig. 7a). Consistently, *E. coli* does not encode HelD, and a distantly related ATPase, RapA, has been proposed to aid RNAP recycling<sup>15</sup>. Unlike HelD, RapA binds near the RNA exit tunnel and does not induce major conformational changes in the EC (Extended Data Fig. 7b). Instead, RapA is thought to rescue ECs by promoting backtracking<sup>35</sup>. Alternative recycling mechanisms likely exist in SI3-containing species. Indeed, *E. coli* DksA has recently been proposed to remove RNAP from nucleic acids<sup>36</sup>. DksA binds in the secondary channel using a Gre-like coiled-coil<sup>37</sup>, induces conformational changes in RNAP<sup>38</sup>, albeit less dramatic than HelD, and is present only in bacteria that have SI3<sup>39</sup>.

The HelD/ $\delta$ -dependent recycling mechanism uncovered here represents a marvelously simple, direct and effective way of recovering RNAP from virtually any state trapped post-termination. However, RNAP is truly recycled only when (i) HelD is released and (ii) cellular conditions support robust RNA synthesis. We show that HelD is released by ATP (Fig. 7b; Extended Data Fig. 6), suggesting that high levels of ATP could help prevent HelD from trapping RNAP in an inactivated complex during exponential growth. Noteworthy, both *B. subtilis* and *M. smegmatis* HelDs cannot bind ATP when fully engaged with RNAP, suggesting that intrinsically timed isomerization into a less engaged conformation must precede ATP binding and release from RNAP. With  $\delta^{\text{CTR}}$  destabilized after HelD release,  $\sigma$  could regenerate ready-to-act holoenzyme.

When cells sporulate during stationary phase, conversely, the levels of ATP are low<sup>40</sup>, transcription is limited, HelD levels match those of RNAP<sup>23</sup>, and HelD is thus expected to remain bound to RNAP. Given that HelD locks RNAP in an inactive state, could it be used to store RNAP until the conditions improve? Intriguingly, we observed RNAP-HelD dimers, suggesting that HelD/ $\delta$  can promote RNAP hibernation that may be essential for fast RNAP recovery, in line with observations that overexpression of HelD enhances sporulation<sup>41</sup> and deletions of HelD,  $\delta$  or both prolong the lag phase<sup>22</sup>. *E. coli* RNAP core also readily forms dimers<sup>9</sup>, and an increased propensity for dimerization and other structural aspects of the RNAP- $\delta$ -HelD complex resemble features of the hibernating eukaryotic RNAP I (Fig. 7c,d). Each protomer of the hibernating RNAP I dimer features a wide open DNA-binding cleft, partially unfolded bridge helix and the DNA-mimicking loop stably bound inside the cleft<sup>32-34</sup>, similar to  $\delta^{\text{CTR}}$ . Moreover, the A12.2 C-terminal domain of RNAP I, which is functionally analogous to Gre factors<sup>32</sup>, is located inside the secondary channel<sup>33</sup>.

Availability of active RNAPs and ribosomes is directly linked to cellular growth and their homeostasis is thus essential for optimal fitness. Syntheses of RNA and protein consume large quantities of ATP and GTP, which fuel many cellular engines and serve as reporters of energy status. Our study suggests that the ribosome and RNAP use analogous strategies to decide whether to hibernate during famine or engage in active polymerization when nutrients are plentiful. Similarly to HelD-trapped RNAP dimers, 100S ribosome dimers are stabilized by hibernation promoting factors (HPF), which also occlude the binding sites for the mRNA template and A- and P-site tRNAs<sup>42-44</sup>. Ribosome revival is mediated by evolutionarily conserved GTPases, such as stress-induced HflX<sup>45,46</sup> or housekeeping EF-G and ribosome recycling factor (RRF), which split the hibernating dimers into 70S monomers in a GTP-dependent fashion<sup>47</sup>, or recycle ribosomes after translation termination<sup>45,48</sup>. Although it is possible that another factor is involved in RNAP reactivation, our results hint that HelD possesses both the post-termination recycling and dimer-promoting activities (Fig. 8).

This one-step mode of regulation is more in line with direct sensing of nucleotides used by RNAP, whereas the ribosome instead relies on a set of translation GTPases. For example, transcription initiation in *E. coli* is adjusted to the growth rate by RNAP binding directly to ATP/GTP in the active site or to the stringent response alarmone (p)ppGpp in an allosteric site<sup>49</sup>. By contrast, the GTP/(p)ppGpp ratio is conveyed to the ribosome by translation initiation factor 2 (IF2), which acts as a metabolic sensor that switches between an active GTP-bound form and an inactive (p)ppGpp-bound form<sup>50</sup>. In either case, the synthetic output is feedback-controlled to ensure optimal fitness and avoid waste of precious resources.

This and the accompanying studies present a hitherto unrecognized transcription recycling system that underpins genome integrity and persistence during periods of dormancy. In our model, reservoirs of active RNAP are controlled by HelD, which directly senses cellular energy charge and may rescue trapped RNAP during fast growth, promote RNAP hibernation during slow growth, and enable efficient RNAP recovery upon shift to a nutrient-rich environment (Fig. 8). We note that although most laboratory experiments are carried out with rapidly growing bacteria for convenience, dormant states are prevalent in natural

environments and pose grave health risks. For example, *B. anthracis* spores are the infectious particles for anthrax, whereas slow-growing *Pseudomonas aeruginosa* biofilms and *M. tuberculosis* are resistant to cidal antibiotics. Unraveling the regulation of dormancy is thus critical for the understanding of bacterial physiology and identifying new strategies for eradication of multidrug-resistant pathogens.

## Methods

### Plasmids, DNAs and RNAs

A DNA fragment encoding *B. subtilis* HelD was PCR-amplified from strain MH5636 (Extended Data Table 1). The PCR product was inserted into expression vector pGEX-6p-1 *via BamHI* and *XhoI* restriction sites, in frame with a region encoding an N-terminal GST-tag. DNA fragments encoding *B. subtilis*  $\sigma^A$ ,  $\delta$  or  $\delta^{\text{NTD}}$  were PCR-amplified from strain MH5636 and inserted into pETM-11 vector (EMBL, Heidelberg) *via NcoI/HindIII* or *NcoI/XhoI* restriction sites, respectively, in frame with a region encoding an N-terminal His<sub>6</sub>-tag. DNA and RNA oligomers used for the assembly of transcription complexes were purchased as single-stranded oligonucleotides (Eurofines and IBA Lifesciences, respectively).

### Protein production and purification

*B. subtilis* strains MH5636, LK782 ( $\Delta\text{helD}$ ) or LK1032 ( $\Delta\text{helD}\Delta\text{rpoE}$ ; Extended Data Table 1) were used to produce stationary phase RNAP, RNAP $^{\Delta\text{HelD}}$  or RNAP $^{\Delta\delta\Delta\text{HelD}}$ , respectively. Chromosomes in these strains are engineered to produce a  $\beta'$  subunit with a C-terminal His<sub>10</sub>-tag. Strains were grown in TB medium at 37 °C to an OD<sub>600</sub> of 1.0 and were then shifted to 18 °C and grown to an OD<sub>600</sub> of about 11. All purification steps were performed at 4 °C. Cells were harvested by centrifugation, resuspended in buffer A (50 mM Na<sub>2</sub>HPO<sub>4</sub>, 300 mM NaCl, 3 mM 2-mercaptoethanol, 5 % [v/v] glycerol, pH 7.9) and lysed by sonication. The lysate was cleared by centrifugation. RNAP variants were captured on Ni<sup>2+</sup>-NTA affinity resin (Macherey-Nagel), washed with buffer A supplemented with 25 mM imidazole and eluted with buffer A supplemented with 250 mM imidazole. The eluate was dialyzed overnight against 50 mM Na<sub>2</sub>HPO<sub>4</sub>, 300 mM NaCl, 3 mM DTT, 5 % [v/v] glycerol, pH 7.9, loaded on a 5 ml HiTrap Heparin HP column (GE Healthcare), washed with buffer B (50 mM TRIS-HCl, 100 mM NaCl, 3 mM DTT, 0.1 mM EDTA, 5 % [v/v] glycerol, pH 7.9) and eluted with a linear gradient to buffer B with 700 mM NaCl. Fractions containing RNAPs were pooled and further purified by SEC on a HiLoad Superdex 200 Increase 16/600 column (GE Healthcare) in 20 mM TRIS-HCl, 150 mM NaCl, 0.5 mM DTT, 5 % (v/v) glycerol, pH 8.0. The final samples were concentrated to approximately 16 mg/ml. RNAP produced from strain MH5636 was directly used for EM sample preparation. Other RNAP preparations were aliquoted, flash frozen in liquid N<sub>2</sub> and stored at -80 °C

Recombinant *B. subtilis* GST-HelD was produced in *Escherichia coli* Rosetta(DE3) cells, His<sub>6</sub>- $\delta$ , His<sub>6</sub>- $\delta^{\text{NTD}}$  and His<sub>6</sub>- $\sigma^A$  were produced in *Escherichia coli* BL21(DE3)-RIL cells. Cells were grown in auto-inducing media<sup>51</sup> at 37 °C to an OD<sub>600</sub> of 1.0 and further incubated at 20 °C overnight. All purification steps were

performed at 4 °C. GST-HelD cells were harvested by centrifugation, resuspended in buffer C (50 mM TRIS-HCl, 500 mM NaCl, 1 mM 2-mercaptoethanol, 10 % [v/v] glycerol, pH 7.9) and lysed by sonication. The lysate was cleared by centrifugation, GST-HelD was captured on glutathione resin (Macherey-Nagel), washed with buffer C and eluted with 50 mM TRIS-HCl, 300 mM NaCl, 1 mM DTT, 10 % (v/v) glycerol, 20 mM reduced glutathione, pH 7.9. Eluted fractions were dialyzed against buffer D (20 mM TRIS-HCl, 200 mM NaCl, 1 mM DTT, 5 % [v/v] glycerol, pH 7.9) in the presence of GST-tagged PreScission protease. HelD was separated from uncleaved protein, GST and GST-PreScission by a second passage through glutathione resin. The flowthrough was further purified by SEC on a HiLoad Superdex 200 Increase 16/600 column equilibrated in buffer D. Fractions containing HelD were concentrated to approximately 15 mg/ml, aliquoted, flash frozen in liquid N<sub>2</sub> and stored at -80 °C.

His<sub>6</sub>-δ or His<sub>6</sub>-δ<sup>NTD</sup> cells were harvested by centrifugation, resuspended in 50 mM TRIS-HCl, 500 mM NaCl, 0.5 mM 2-mercaptoethanol 5 % [v/v] glycerol, pH 6.0, and lysed by sonication. The lysate was cleared by centrifugation, His<sub>6</sub>-δ/His<sub>6</sub>-δ<sup>NTD</sup> was captured on Ni<sup>2+</sup>-NTA resin, washed with 50 mM TRIS-HCl, 300 mM NaCl, 0.5 mM 2-mercaptoethanol, 10 mM imidazole, 5 % (v/v) glycerol, pH 6.0, and eluted with 20 mM TRIS-HCl, 150 mM NaCl, 0.5 mM 2-mercaptoethanol, 400 mM imidazole, 5 % (v/v) glycerol, pH 6.0. For the assembly of complexes for cryoEM analysis, eluted His<sub>6</sub>-δ was supplemented with His-tagged TEV protease (1:40 [w/w]), dialyzed against buffer E (20 mM TRIS-HCl, 150 mM NaCl, 1 mM DTT, 5 % (v/v) glycerol, pH 6.0) overnight and passed through fresh Ni<sup>2+</sup>-NTA resin to remove uncleaved His<sub>6</sub>-δ, cleaved His<sub>6</sub>-tag His-tagged TEV protease. Proteins were further purified by SEC on a Superdex75 Increase 10/300 column (GE Healthcare) in buffer E. Fractions containing His<sub>6</sub>-δ, δ or His<sub>6</sub>-δ<sup>NTD</sup> were concentrated to approximately 4 mg/ml (His<sub>6</sub>-δ, His<sub>6</sub>-δ<sup>NTD</sup>) and 23 mg/ml (δ), aliquoted, flash frozen in liquid N<sub>2</sub> and stored at -80 °C.

σ<sup>A</sup> cells were harvested by centrifugation, resuspended in buffer F (20 mM TRIS-HCl, 500 mM NaCl, 1 mM 2-mercaptoethanol, 5 % [v/v] glycerol, pH 7.5) supplemented with 20 mM imidazole, and lysed by sonication. The lysate was cleared by centrifugation, His<sub>6</sub>-σ<sup>A</sup> was captured on Ni<sup>2+</sup>-NTA resin, washed with buffer F supplemented with 50 mM imidazole, and eluted with buffer F supplemented with 400 mM imidazole. Eluted His<sub>6</sub>-σ<sup>A</sup> was supplemented with His-tagged TEV protease (1:40 [w/w]), dialyzed against buffer F supplemented with 1 mM EDTA overnight and passed through fresh Ni<sup>2+</sup>-NTA resin to remove uncleaved His<sub>6</sub>-σ<sup>A</sup>, cleaved His<sub>6</sub>-tag and His-tagged TEV protease. The target protein was further purified by SEC on a Superdex75 Increase 16/600 column (GE Healthcare) in 25 mM TRIS-HCl, 300 mM NaCl, 0.1 mM DTT, 5 % (v/v) glycerol, pH 7.5. Fractions containing σ<sup>A</sup> were concentrated to approximately 39 mg/ml, aliquoted, flash frozen in liquid N<sub>2</sub> and stored at -80 °C.

### **Crosslinking/mass spectrometry**

Sulfo-SDA predominantly establishes lysine-X crosslinks through a primary amine-reactive moiety on one side and a UV-activatable moiety on the other (theoretical crosslinking limit 25 Å). Sulfo-SDA was

prepared at 3 mg/ml in 20 mM HEPES-NaOH, 5 mM Mg(OAc)<sub>2</sub>, 300 mM NaCl, 5 mM DTT, 5% (v/v) glycerol, pH 8.0 immediately prior to addition of RNAP<sup>ΔΔHelD</sup>, RNAP<sup>ΔΔHelD-δ</sup>, RNAP<sup>ΔΔHelD</sup>-HelD or RNAP<sup>ΔΔHelD-δ</sup>-HelD (protein:sulfo-SDA 1:3 [w/w]). Samples were incubated on ice for two hours and then irradiated in a thin film using 365 nm UV irradiation (UVP CL-1000 UV Crosslinker, UVP Inc.) for 20 min on ice (5 cm distance from UV-A lamp). The crosslinked samples were separated by 4-12 % BIS-TRIS NuPAGE, gel bands corresponding to crosslinked monomeric complexes were excised and digested in-gel as described previously<sup>52</sup> Resulting peptides were desalted using C18 StageTips<sup>53</sup>.

10 % of each sample were analyzed by LC-MS/MS without fractionation, the remaining 90 % were fractionated using SEC on a Superdex Peptide 3.2/300 column (GE Healthcare) in 30 % (v/v) acetonitrile, 0.1 % (v/v) trifluoroacetic acid at a flow rate of 10 μl/min to enrich for crosslinked peptides<sup>54</sup>. The first six peptide-containing fractions (50 μl each) were collected, solvent was removed using a vacuum concentrator and the fractions were analyzed by LC-MS/MS on an Orbitrap Fusion Lumos Tribrid mass spectrometer (Thermo Fisher Scientific), connected to an Ultimate 3000 RSLCnano system (Dionex, Thermo Fisher Scientific).

The non-fractionated samples were injected onto a 50 cm EASY-Spray C18 LC column (Thermo Fisher Scientific) operated at 50 °C. Peptides were separated using a linear gradient going from 2 % mobile phase B (80 % [v/v] acetonitrile, 0.1 % [v/v] formic acid) to 40 % mobile phase B in mobile phase A (0.1 % [v/v] formic acid) at a flow rate of 0.3 μl/min over 110 minutes, followed by a linear increase from 40 % to 95 % mobile phase B in 11 minutes. Eluted peptides were ionized by an EASY-Spray source (Thermo Fisher Scientific) and MS data were acquired in the data-dependent mode with the top-speed option. For each three-second acquisition cycle, the full scan mass spectrum was recorded in the Orbitrap with a resolution of 120,000. The ions with a charge state from 3+ to 7+ were isolated and fragmented using higher-energy collisional dissociation (HCD) with 30 % collision energy. The fragmentation spectra were then recorded in the Orbitrap with a resolution of 50,000. Dynamic exclusion was enabled with single repeat count and 60 s exclusion duration.

SEC fractions were analyzed using an identical LC-MS/MS setup. Peptides were separated by applying a gradient ranging from 2 % to 45 % mobile phase B (optimized for each fraction) over 90 min, followed by ramping up mobile phase B to 55 % and 95 % within 2.5 min each. For each three-second data-dependent MS acquisition cycle, the full scan mass spectrum was recorded in the Orbitrap with a resolution of 120,000. The ions with a charge state from 3+ to 7+ were isolated and fragmented using HCD. For each isolated precursor, one of three collision energy settings (26 %, 28 % or 30 %) was selected for fragmentation using a data-dependent decision tree based on the m/z and charge of the precursor. The fragmentation spectra were recorded in the Orbitrap with a resolution of 50,000. Dynamic exclusion was enabled with single repeat count and 60 s exclusion duration.

LC-MS/MS data generated from the four complexes were processed separately. MS2 peak lists were generated from the raw MS data files using the MSConvert module in ProteoWizard (version 3.0.11729). The default parameters were applied, except that Top MS/MS Peaks per 100 Da was set to 20 and the

denoising function was enabled. Precursor and fragment  $m/z$  values were recalibrated. Identification of crosslinked peptides was carried out using xiSEARCH software (<https://www.rappsilberlab.org/software/xisearch>; version 1.7.4)<sup>55</sup>. For RNAP $\Delta\delta\Delta$ HelD, peak lists were searched against the sequence and the reversed sequence of RNAP subunits ( $\alpha$ ,  $\beta$ ,  $\beta'$  and  $\epsilon$ ) and two co-purified proteins,  $\sigma^A$  and  $\sigma^B$ . For RNAP $\Delta\delta\Delta$ HelD- $\delta$ , RNAP $\Delta\delta\Delta$ HelD-HelD and RNAP $\Delta\delta\Delta$ HelD- $\delta$ -HelD samples, protein sequences of  $\delta$ , HelD or both were included in the database. The following parameters were applied for the search: MS accuracy = 4 ppm; MS2 accuracy = 8 ppm; enzyme = trypsin (with full tryptic specificity); allowed number of missed cleavages = 2; missing monoisotopic peak = 2; crosslinker = sulfo-SDA (the reaction specificity for sulfo-SDA was assumed to be for lysine, serine, threonine, tyrosine and protein N termini on the NHS ester end, and any amino acid residue for the diazirine end); fixed modifications = carbamidomethylation on cysteine; variable modifications = oxidation on methionine and sulfo-SDA loop link. Identified crosslinked peptide candidates were filtered using xiFDR<sup>56</sup>. A false discovery rate of 5 % on residue-pair level was applied with the “boost between” option selected. Crosslinked residue pairs identified from the four complexes are summarized in Extended Data Table 4 and Supplementary Table 1.

### Cryo-EM data collection and processing

Equimolar amounts of tDNA, ntDNA and RNA were mixed in buffer G (20 mM TRIS-HOAc, 5 mM Mg[OAc]<sub>2</sub>, 100 mM KOAc, 2 mM DTT, 5 % [v/v] glycerol, pH 8.0) and annealed by heating to 95 °C for 5 min and subsequent cooling to 25 °C at 1 °C/min. The annealed scaffold was incubated with *B. subtilis* RNAP in a 1.3:1 molar ratio in buffer H (20 mM TRIS-HOAc, 5 mM Mg[OAc]<sub>2</sub>, 300 mM KOAc, 2 mM DTT, 5 % [v/v] glycerol, pH 8.0) for 10 min on ice, then for 10 min at 32 °C. Equimolar amounts (to RNAP) of  $\delta$  and HelD were added stepwise, followed by incubation for 10 min at 32 °C after each addition. The mixture was subjected to SEC on a Superdex 200 Increase 3.2/300 column (GE Healthcare) in buffer H. Fractions containing RNAP,  $\delta$  and HelD were pooled and concentrated to approximately 5 mg/ml.

Immediately before preparation of the grids, the sample was supplemented with 0.15 % (w/v) n-octylglucoside. 3.8  $\mu$ l of the final mixture were spotted on plasma-treated Quantifoil R1/2 holey carbon grids at 10 °C/100 % humidity, and plunged into liquid ethane using a FEI Vitrobot Mark IV. Image acquisition was conducted on a FEI Titan Krios G3i (300 kV) with a Falcon 3EC camera at a nominal magnification of 92,000 in counting mode using EPU software (Thermo Fisher Scientific) with a calibrated pixel size of 0.832 Å. A total electron dose of 40 e/Å<sup>2</sup> was accumulated over an exposure time of 36 s. Movie alignment was done with MotionCor2<sup>57</sup> using 5x5 patches followed by ctf estimation with Gctf<sup>58</sup>.

All following image analysis steps were done with cryoSPARC<sup>59</sup>. Class averages of manually selected particles were used to generate an initial template for reference-based particle picking from 9,127 micrographs. Particle images were extracted with a box size of 440 and binned to 110 for initial analysis. *Ab initio* reconstruction using a small subset of particles was conducted to generate an initial 3D

reference for 3D heterogeneous refinement. The dataset was iteratively classified into two well-resolved populations representing monomeric and dimeric RNAP- $\delta$ -HelD. Selected particles were re-extracted with a box of 220 and again classified in 3D to further clean the dataset. Finally, selected particle images were re-extracted with a box of 280 (1.3 Å/px) and subjected to local refinement using a generously enlarged soft-mask for monomeric or dimeric RNAP- $\delta$ -HelD. Local refinement of the dimer particles using the monomeric mask was conducted as a control to trace differences of RNAP- $\delta$ -HelD in the authentic monomer and dimer structures. After per-particle CTF correction, non-uniform refinement was applied to generate the final reconstructions.

## Model building and refinement

The final cryoEM map for the dimeric RNAP- $\delta$ -HelD complex (Extended Data Fig. 3) was used for initial model building. Coordinates of *M. smegmatis* RNAP  $\alpha$ ,  $\beta$  and  $\beta'$  subunits (PDB ID 5VI8)<sup>60</sup> were docked into the cryoEM map using Coot<sup>61</sup>. Modeling of  $\delta$  was based on the NMR structure of *B. subtilis*  $\delta$  (PDB ID 2M4K)<sup>62</sup>. Modeling of  $\epsilon$  was supported by the structure of YkzG from *Geobacillus stearothermophilus* (PDB ID 4NJC)<sup>19</sup>. Model building of HelD was supported by the structure of UvrD helicase from *E. coli* (PDB ID 3LFU)<sup>63</sup> as well as the C-terminal domain of a putative DNA helicase from *Lactobacillus plantarum* (PDB ID 3DMN). The subunits were manually rebuilt into the cryoEM map. The model was completed and manually adjusted residue-by-residue, supported by real space refinement in Coot. The manually built model was refined against the cryoEM map using the real space refinement protocol in PHENIX<sup>64</sup>. Model building of the monomeric complex was done in the same way but starting with a model of half of the dimeric complex. The structures were evaluated with Molprobit<sup>65</sup>. Structure figures were prepared using PyMOL (Version 1.8 Schrödinger, LLC).

## Structure comparisons

Structures were compared by global superposition of complex structures or by superposition of selected subunits in complexes using the “secondary structure matching” algorithm implemented in Coot or the “align” algorithm implemented in PyMOL.

## Size exclusion chromatography/multi-angle light scattering

SEC/MALS analysis was performed on an HPLC system (Agilent) coupled to mini DAWN TREOS multi-angle light scattering and RefractoMax 520 refractive index detectors (Wyatt Technology). RNAP- $\delta$ -HelD complex was assembled as for cryoEM. 60  $\mu$ l of the sample at 1 mg/ml were chromatographed on a Superose 6 Increase 10/300 column (GE Healthcare) in buffer H supplemented with 0.02 % (w/v)  $\text{NaN}_3$  at 18 °C with a flowrate of 0.6 ml/min. Data were analyzed with the ASTRA 6.1 software (Wyatt Technology) using monomeric bovine serum albumin (Sigma-Aldrich) as a reference.

## Interaction assays

HeID interactions with  $\delta$  or  $\delta^{\text{NTD}}$  were analyzed by analytical SEC. 21  $\mu\text{M}$  HeID and 42  $\mu\text{M}$   $\delta$  or  $\delta^{\text{NTD}}$  were mixed in 20 mM HEPES-NaOH, 50 mM NaCl, 1 mM DTT, pH 7.5, and incubated for 10 min at room temperature. 50  $\mu\text{l}$  of the samples were loaded on a Superdex S200 Increase PC 3.2 column (GE Healthcare) and chromatographed at 4 °C with a flow rate of 40  $\mu\text{l}/\text{min}$ . Fractions were analyzed by 12.5 % SDS PAGE.

### **Electrophoretic gel mobility shift assays**

Equimolar amounts of 5'-[ $^{32}\text{P}$ ]-labeled tDNA and unlabeled ntDNA were mixed in buffer G and annealed by heating to 95 °C for 5 min and subsequent cooling to 25 °C at 1 °C/min. 1  $\mu\text{M}$  each of HeID,  $\delta$ , RNAP $\Delta\delta\Delta\text{HeID}$ , RNAP $\Delta\delta\Delta\text{HeID}/\text{HeID}$ , RNAP $\Delta\delta\Delta\text{HeID}/\delta$  or 1  $\mu\text{M}$  RNAP $\Delta\delta\Delta\text{HeID}/\text{HeID}$  and increasing amounts of  $\delta$  or  $\delta^{\text{NTD}}$  were mixed with 5 nM of the labeled duplex, and incubated in buffer H for 10 min at 4 °C followed by 10 min at 32 °C. Samples were loaded on a 4 % native PAGE gel and electrophoresed in 0.5X TBE buffer. Radioactive bands were visualized using a Storm phosphorimager and quantified using ImageQuant software (GE Healthcare).

### **HeID release assays**

Equimolar amounts of HeID and stationary phase RNAP were mixed in buffer I (20 mM TRIS-HCl, 300 mM NaCl, 2 mM DTT, 5 % (v/v) glycerol, pH 8.0), incubated for 10 min on ice and then for 10 min at 32 °C. The sample was chromatographed on a HiLoad Superdex 200 Increase 10/300 column (GE Healthcare) in buffer I. Fractions were analyzed by 12.5 % SDS PAGE, fractions containing RNAP-HeID complex were collected and concentrated to approximately 3 mg/ml (6.7  $\mu\text{M}$ ). 80  $\mu\text{l}$  6.7  $\mu\text{M}$  complex were mixed with buffer I, 5 mM  $\text{Mg}^{2+}$ -ATP $\gamma\text{S}$ /AMPPNP/ATP/ADP/AMP, 6.7  $\mu\text{M}$   $\sigma^{\text{A}}$  or  $\sigma^{\text{A}}$  plus  $\text{Mg}^{2+}$ -ATP $\gamma\text{S}$  in buffer I. 90  $\mu\text{l}$  of the samples were loaded on a Superdex S200 Increase PC 3.2 column (GE Healthcare) and chromatographed at 4 °C with a flow rate of 40  $\mu\text{l}/\text{min}$ . Fractions were analyzed by 12.5 % SDS PAGE.

## **Declarations**

### **Reporting summary**

Further information on research design is available in the Nature Research Reporting Summary linked to this paper.

### **Data availability**

CryoEM maps were deposited in the Electron Microscopy Data Bank (<https://www.ebi.ac.uk/pdbe/emdb/>) under accession codes EMD-11104 (monomeric RNAP- $\delta$ -HeID) and EMD-11105 (dimeric RNAP- $\delta$ -HeID), and will be released upon publication. Structure coordinates have been deposited in the RCSB Protein Data Bank (<https://www.rcsb.org/>) with accession codes 6ZCA (monomeric RNAP- $\delta$ -HeID) and 6ZFB

(dimeric RNAP- $\delta$ -Held), and will be released upon publication. CLMS data have been deposited in jPOST (<https://jpostdb.org/>) with accession code JPST000858/PXD019437 (<https://repository.jpostdb.org/preview/11873847225ed4c61c43749>; access key 3884) and will be released upon publication. All other data supporting the findings of this study are available from the corresponding author on request.

## Acknowledgements

We are grateful to Dr. John D. Helmann for valuable comments. *B. subtilis* strains MH5636, LK782 ( $\Delta$ held) or LK1032 ( $\Delta$ held $\Delta$ rpoE) were a kind gift from Libor Krásný, Czech Academy of Sciences. We thank Nicole Dimos, Freie Universität Berlin, for help in RNAP purification, Christoph Weise, Freie Universität Berlin, for MS-based fingerprinting, and Boris Schade and Benedikt Kirmayer for assistance in cryoEM. We acknowledge access to electron microscopic equipment at the core facility BioSupraMol of Freie Universität Berlin, supported through grants from the Deutsche Forschungsgemeinschaft and the state of Berlin for large equipment according to Art. 91b GG (INST 335/588-1 FUGG, INST 335/589-1 FUGG, INST 335/590-1 FUGG). We are grateful for access to high-performance computing resources at the Zuse Institut Berlin. This work was supported by grants from the Deutsche Forschungsgemeinschaft (SFB 973/C08 and 433623608 to M.C.W.; GRK 2473 to M.C.W. and J.R.), the National Institutes of Health (GM067153 to I.A.), the Sigrid Jusélius Foundation to G.A.B.), and by the Wellcome Trust through a Senior Research Fellowship to JR (103139). The Wellcome Centre for Cell Biology is supported by core funding from the Wellcome Trust (203149). H.-H.P. was sponsored by a PhD fellowship from the Chinese Fellowship Council. Y.-H.H. was sponsored by a PhD fellowship from the Chinese Fellowship Council and by a postdoctoral fellowship from the Collaborative Research Center 973 of the Deutsche Forschungsgemeinschaft.

## Author information

### Affiliations

*Laboratory of Structural Biochemistry, Freie Universität Berlin, Berlin, Germany*

Hao-Hong Pei

Yong-Heng Huang

Nelly Said

Bernhard Loll

Markus C. Wahl

*Research Center of Electron Microscopy and Core Facility BioSupraMol, Freie Universität Berlin, Berlin, Germany*

Tarek Hilal

*Bioanalytics, Technische Universität Berlin, Gustav-Meyer-Allee 25, 13355 Berlin Berlin, Germany*

Zhuo A. Chen

Juri Rappsilber

*Wellcome Centre for Cell Biology, University of Edinburgh, Edinburgh EH9 3BF, UK*

Juri Rappsilber

*Department of Biochemistry, University of Turku, FIN-20014 Turku, Finland*

Georgiy A. Belogurov

*Department of Microbiology and Center for RNA Biology, The Ohio State University, Columbus, OH, USA*

Irina Artsimovitch

*Macromolecular Crystallography, Helmholtz-Zentrum Berlin für Materialien und Energie, Berlin, Germany*

Markus C. Wahl

### **Author contributions**

H.-H.P. cloned genes, produced proteins/complexes and performed experiments with help from Y.-H.H., Y.G., and N.S., prepared cryoEM samples with T.H., built atomic models with B.L. and M.C.W., refined structures with B.L. and performed crosslinking with Z.A.C.. T.H., acquired, processed and refined cryoEM data. Z.A.C. performed CLMS analyses. All authors contributed to the analysis of the data and the interpretation of the results. M.C.W., I.A. and G.B. wrote the manuscript with contributions from the other authors. J.R. and M.C.W. supervised work in their respective groups. M.C.W. conceived and coordinated the project.

### **Corresponding author**

Correspondence to Markus C. Wahl.

### **Ethics declarations**

### **Competing interests**

The authors declare no competing interests.

### **Additional information**

**Supplementary Information** is available for this paper at ....

Correspondence and requests for materials should be addressed to M.C.W..

Reprints and permissions information is available at [www.nature.com/reprints](http://www.nature.com/reprints).

## References

1. Helmann, J.D. Where to begin? Sigma factors and the selectivity of transcription initiation in bacteria. *Mol Microbiol* (2019).
2. Peters, J.M., Vangeloff, A.D. & Landick, R. Bacterial transcription terminators: the RNA 3'-end chronicles. *J Mol Biol* **412**, 793-813 (2011).
3. Kang, W. et al. Transcription reinitiation by recycling RNA polymerase that diffuses on DNA after releasing terminated RNA. *Nat Commun* **11**, 450 (2020).
4. Bellecourt, M.J., Ray-Soni, A., Harwig, A., Mooney, R.A. & Landick, R. RNA Polymerase Clamp Movement Aids Dissociation from DNA but Is Not Required for RNA Release at Intrinsic Terminators. *J Mol Biol* **431**, 696-713 (2019).
5. Harden, T.T. et al. Alternative transcription cycle for bacterial RNA polymerase. *Nat Commun* **11**, 448 (2020).
6. Washburn, R.S. & Gottesman, M.E. Transcription termination maintains chromosome integrity. *Proc Natl Acad Sci U S A* **108**, 792-7 (2011).
7. Lopez de Saro, F.J., Woody, A.Y. & Helmann, J.D. Structural analysis of the *Bacillus subtilis* delta factor: a protein polyanion which displaces RNA from RNA polymerase. *J Mol Biol* **252**, 189-202 (1995).
8. Altmann, C.R., Solow-Cordero, D.E. & Chamberlin, M.J. RNA cleavage and chain elongation by *Escherichia coli* DNA-dependent RNA polymerase in a binary enzyme-RNA complex. *Proc Natl Acad Sci U S A* **91**, 3784-8 (1994).
9. Busby, S., Spassky, A. & Buc, H. On the binding of tRNA to *Escherichia coli* RNA polymerase. Interactions between the core enzyme, DNA and tRNA. *Eur J Biochem* **118**, 443-51 (1981).
10. Wassarman, K.M. & Saecker, R.M. Synthesis-mediated release of a small RNA inhibitor of RNA polymerase. *Science* **314**, 1601-3 (2006).
11. Epshtein, V., Cardinale, C.J., Ruckenstein, A.E., Borukhov, S. & Nudler, E. An allosteric path to transcription termination. *Molecular Cell* **28**, 991-1001 (2007).
12. Travers, A. RNA polymerase specificity and the control of growth. *Nature* **263**, 641-6 (1976).
13. Gohara, D.W. & Yap, M.F. Survival of the drowsiest: the hibernating 100S ribosome in bacterial stress management. *Curr Genet* **64**, 753-760 (2018).
14. Selby, C.P. Mfd Protein and Transcription-Repair Coupling in *Escherichia coli*. *Photochem Photobiol* **93**, 280-295 (2017).
15. Sukhodolets, M.V., Cabrera, J.E., Zhi, H. & Jin, D.J. RapA, a bacterial homolog of SWI2/SNF2, stimulates RNA polymerase recycling in transcription. *Genes Dev* **15**, 3330-41 (2001).

16. Juang, Y.L. & Helmann, J.D. The delta subunit of *Bacillus subtilis* RNA polymerase. An allosteric effector of the initiation and core-recycling phases of transcription. *J Mol Biol* **239**, 1-14 (1994).
17. Rabatinova, A. et al. The delta subunit of RNA polymerase is required for rapid changes in gene expression and competitive fitness of the cell. *J Bacteriol* **195**, 2603-11 (2013).
18. Williamson, V.M. & Doi, R.H. Delta factor can displace sigma factor from *Bacillus subtilis* RNA polymerase holoenzyme and regulate its initiation activity. *Mol Gen Genet* **161**, 135-41 (1978).
19. Keller, A.N. et al. epsilon, a new subunit of RNA polymerase found in gram-positive bacteria. *J Bacteriol* **196**, 3622-32 (2014).
20. Koval, T. et al. Domain structure of HelD, an interaction partner of *Bacillus subtilis* RNA polymerase. *FEBS Lett* **593**, 996-1005 (2019).
21. Carrasco, B., Fernandez, S., Petit, M.A. & Alonso, J.C. Genetic recombination in *Bacillus subtilis* 168: effect of DeltahelD on DNA repair and homologous recombination. *J Bacteriol* **183**, 5772-7 (2001).
22. Wiedermannova, J. et al. Characterization of HelD, an interacting partner of RNA polymerase from *Bacillus subtilis*. *Nucleic Acids Res* **42**, 5151-63 (2014).
23. Nicolas, P. et al. Condition-dependent transcriptome reveals high-level regulatory architecture in *Bacillus subtilis*. *Science* **335**, 1103-6 (2012).
24. Kang, J.Y. et al. Structural basis of transcription arrest by coliphage HK022 Nun in an *Escherichia coli* RNA polymerase elongation complex. *Elife* **6**, e25478 (2017).
25. Hirata, A., Klein, B.J. & Murakami, K.S. The X-ray crystal structure of RNA polymerase from Archaea. *Nature* **451**, 851-4 (2008).
26. de Jong, L. et al. In-Culture Cross-Linking of Bacterial Cells Reveals Large-Scale Dynamic Protein-Protein Interactions at the Peptide Level. *J Proteome Res* **16**, 2457-2471 (2017).
27. Lee, J.Y. & Yang, W. UvrD helicase unwinds DNA one base pair at a time by a two-part power stroke. *Cell* **127**, 1349-60 (2006).
28. Abdelkareem, M. et al. Structural Basis of Transcription: RNA Polymerase Backtracking and Its Reactivation. *Mol Cell* **75**, 298-309 e4 (2019).
29. Belogurov, G.A. & Artsimovitch, I. The Mechanisms of Substrate Selection, Catalysis, and Translocation by the Elongating RNA Polymerase. *J Mol Biol* **431**, 3975-4006 (2019).
30. Kouba, T. et al. The Core and Holoenzyme Forms of RNA Polymerase from *Mycobacterium smegmatis*. *J Bacteriol* **201**(2019).
31. Park, J.S. & Roberts, J.W. Role of DNA bubble rewinding in enzymatic transcription termination. *Proc Natl Acad Sci U S A* **103**, 4870-5 (2006).
32. Fernandez-Tornero, C. et al. Crystal structure of the 14-subunit RNA polymerase I. *Nature* **502**, 644-9 (2013).
33. Fernandez-Tornero, C. RNA polymerase I activation and hibernation: unique mechanisms for unique genes. *Transcription* **9**, 248-254 (2018).

34. Neyer, S. et al. Structure of RNA polymerase I transcribing ribosomal DNA genes. *Nature* **540**, 607-610 (2016).
35. Liu, B., Zuo, Y. & Steitz, T.A. Structural basis for transcription reactivation by RapA. *Proc Natl Acad Sci U S A* **112**, 2006-10 (2015).
36. Myka, K.K. & Gottesman, M.E. DksA and DNA double-strand break repair. *Curr Genet* **65**, 1297-1300 (2019).
37. Perederina, A. et al. Regulation through the secondary channel–structural framework for ppGpp-DksA synergism during transcription. *Cell* **118**, 297-309 (2004).
38. Molodtsov, V. et al. Allosteric Effector ppGpp Potentiates the Inhibition of Transcript Initiation by DksA. *Mol Cell* **69**, 828-839 e5 (2018).
39. Furman, R., Tsodikov, O.V., Wolf, Y.I. & Artsimovitch, I. An insertion in the catalytic trigger loop gates the secondary channel of RNA polymerase. *J Mol Biol* **425**, 82-93 (2013).
40. Hutchison, K.W. & Hanson, R.S. Adenine nucleotide changes associated with the initiation of sporulation in *Bacillus subtilis*. *J Bacteriol* **119**, 70-5 (1974).
41. Meeske, A.J. et al. High-Throughput Genetic Screens Identify a Large and Diverse Collection of New Sporulation Genes in *Bacillus subtilis*. *PLoS Biol* **14**, e1002341 (2016).
42. Beckert, B. et al. Structure of the *Bacillus subtilis* hibernating 100S ribosome reveals the basis for 70S dimerization. *EMBO J* **36**, 2061-2072 (2017).
43. Beckert, B. et al. Structure of a hibernating 100S ribosome reveals an inactive conformation of the ribosomal protein S1. *Nat Microbiol* **3**, 1115-1121 (2018).
44. Khusainov, I. et al. Structures and dynamics of hibernating ribosomes from *Staphylococcus aureus* mediated by intermolecular interactions of HPF. *EMBO J* **36**, 2073-2087 (2017).
45. Zhang, Y. et al. HflX is a ribosome-splitting factor rescuing stalled ribosomes under stress conditions. *Nat Struct Mol Biol* **22**, 906-13 (2015).
46. Basu, A. & Yap, M.N. Disassembly of the *Staphylococcus aureus* hibernating 100S ribosome by an evolutionarily conserved GTPase. *Proc Natl Acad Sci U S A* **114**, E8165-E8173 (2017).
47. Basu, A., Shields, K.E. & Yap, M.F. The hibernating 100S complex is a target of ribosome-recycling factor and elongation factor G in *Staphylococcus aureus*. *J Biol Chem* **295**, 6053-6063 (2020).
48. Hirokawa, G., Iwakura, N., Kaji, A. & Kaji, H. The role of GTP in transient splitting of 70S ribosomes by RRF (ribosome recycling factor) and EF-G (elongation factor G). *Nucleic Acids Res* **36**, 6676-87 (2008).
49. Gourse, R.L. et al. Transcriptional Responses to ppGpp and DksA. *Annu Rev Microbiol* **72**, 163-184 (2018).
50. Milon, P. et al. The nucleotide-binding site of bacterial translation initiation factor 2 (IF2) as a metabolic sensor. *Proc Natl Acad Sci U S A* **103**, 13962-7 (2006).
51. Studier, F.W. Protein production by auto-induction in high-density shaking cultures. *Protein Express Purif* **41**, 207-234 (2005).

52. Chen, Z.A. et al. Architecture of the RNA polymerase II-TFIIF complex revealed by cross-linking and mass spectrometry. *EMBO J* **29**, 717-26 (2010).
53. Rappsilber, J., Mann, M. & Ishihama, Y. Protocol for micro-purification, enrichment, pre-fractionation and storage of peptides for proteomics using StageTips. *Nat Protoc* **2**, 1896-906 (2007).
54. Leitner, A., Walzthoeni, T. & Aebersold, R. Lysine-specific chemical cross-linking of protein complexes and identification of cross-linking sites using LC-MS/MS and the xQuest/xProphet software pipeline. *Nat Protoc* **9**, 120-37 (2014).
55. Mendes, M.L. et al. An integrated workflow for crosslinking mass spectrometry. *Mol Syst Biol* **15**, e8994 (2019).
56. Fischer, L. & Rappsilber, J. Quirks of Error Estimation in Cross-Linking/Mass Spectrometry. *Anal Chem* **89**, 3829-3833 (2017).
57. Zheng, S.Q. et al. MotionCor2: anisotropic correction of beam-induced motion for improved cryo-electron microscopy. *Nat Methods* **14**, 331-332 (2017).
58. Zhang, K. Gctf: Real-time CTF determination and correction. *J Struct Biol* **193**, 1-12 (2016).
59. Punjani, A., Rubinstein, J.L., Fleet, D.J. & Brubaker, M.A. cryoSPARC: algorithms for rapid unsupervised cryo-EM structure determination. *Nat Methods* **14**, 290-296 (2017).
60. Hubin, E.A., Lilic, M., Darst, S.A. & Campbell, E.A. Structural insights into the mycobacteria transcription initiation complex from analysis of X-ray crystal structures. *Nat Commun* **8**, 16072 (2017).
61. Emsley, P., Lohkamp, B., Scott, W.G. & Cowtan, K. Features and development of Coot. *Acta Crystallogr D* **66**, 486-501 (2010).
62. Papouskova, V. et al. Structural study of the partially disordered full-length delta subunit of RNA polymerase from *Bacillus subtilis*. *Chembiochem* **14**, 1772-9 (2013).
63. Jia, H. et al. Rotations of the 2B sub-domain of *E. coli* UvrD helicase/translocase coupled to nucleotide and DNA binding. *J Mol Biol* **411**, 633-48 (2011).
64. Afonine, P.V. et al. Towards automated crystallographic structure refinement with phenix.refine. *Acta Crystallogr D* **68**, 352-367 (2012).
65. Williams, C.J. et al. MolProbity: More and better reference data for improved all-atom structure validation. *Protein Sci* **27**, 293-315 (2018).
66. Qi, Y. & Hulett, F.M. PhoP-P and RNA polymerase sigmaA holoenzyme are sufficient for transcription of Pho regulon promoters in *Bacillus subtilis*: PhoP-P activator sites within the coding region stimulate transcription in vitro. *Mol Microbiol* **28**, 1187-97 (1998).

## Additional File Legends

### Supplementary Tables

#### Supplementary Table 1.

Inter-molecular crosslinks in RNAP<sup>ΔδΔHelD</sup>, RNAP<sup>ΔδΔHelD</sup>-δ, RNAP<sup>ΔδΔHelD</sup>-HelD and RNAP<sup>ΔδΔHelD</sup>-δ-HelD.

## Supplementary Data

### Supplementary Data 1.

Interactive 3D illustration of the overall architecture of a monomeric RNAP-δ-HelD complex:

[https://belogurov.org/held/monomer\\_overview\\_legend.html](https://belogurov.org/held/monomer_overview_legend.html)

### Supplementary Data 2.

Interactive 3D illustration of the RNAP-δ-HelD complex with overlaid DNA/RNA from *E. coli* EC:

[https://belogurov.org/held/monomer\\_TEC\\_super.html](https://belogurov.org/held/monomer_TEC_super.html)

### Supplementary Data 3.

Interactive 3D illustration of the overall architecture of a dimeric RNAP-δ-HelD complex:

[https://belogurov.org/held/dimer\\_overview\\_legend.html](https://belogurov.org/held/dimer_overview_legend.html)

## Figures

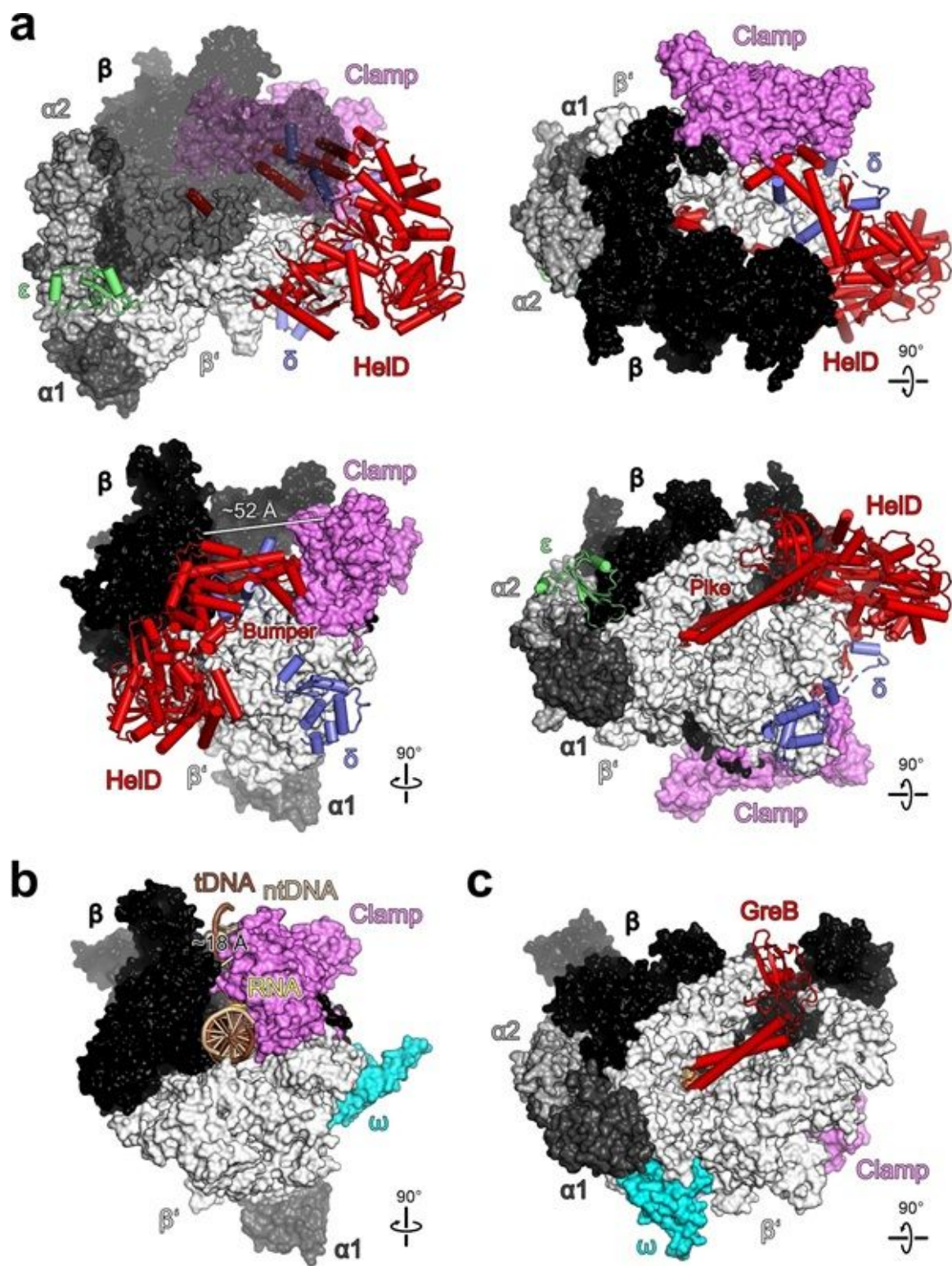
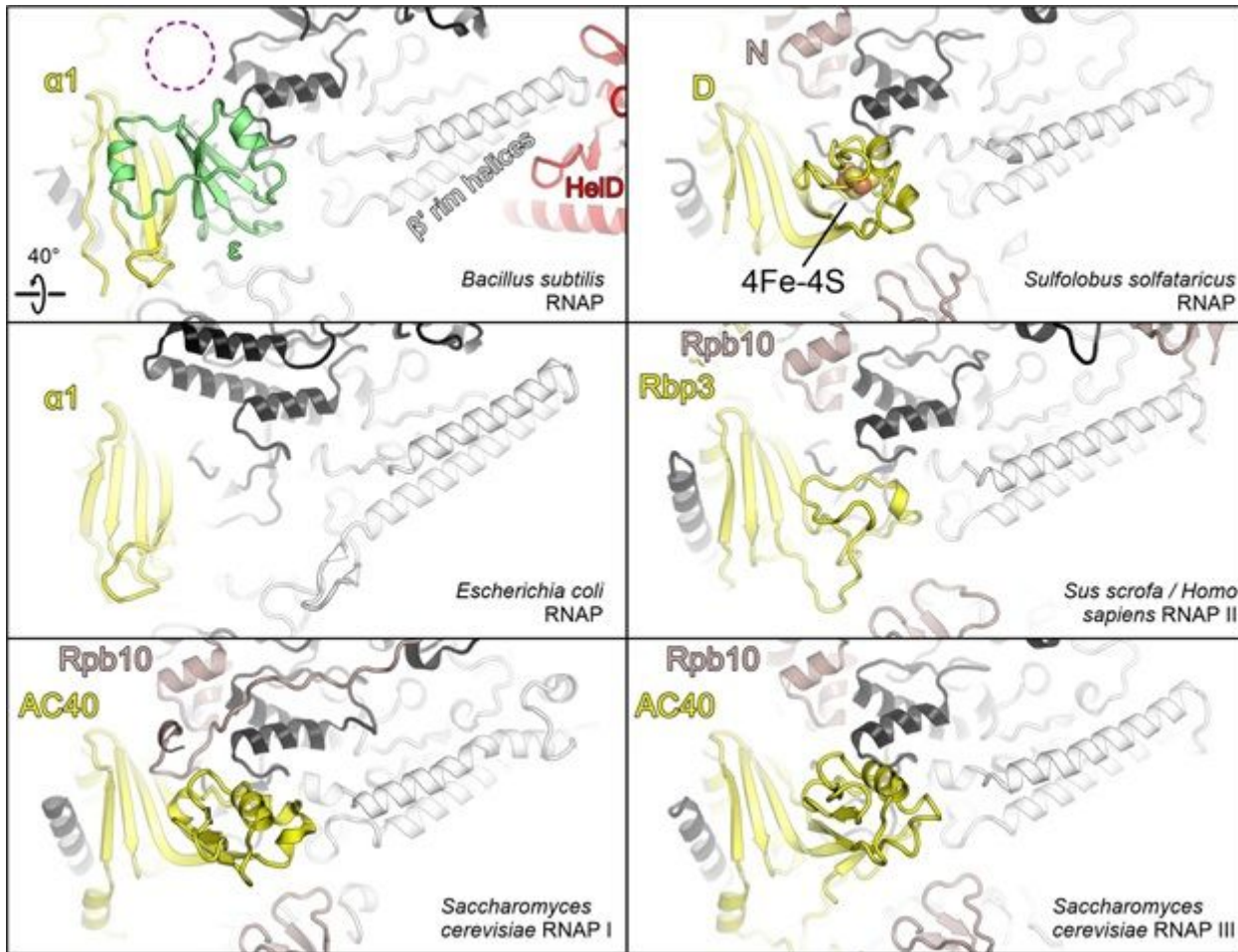


Figure 1

Structural overview. a, Overall architecture of a RNAP- $\delta$ -HelD complex.  $\beta$  surface is semi-transparent in the upper left panel. Rotation symbols in this and all figures indicate views relative to the upper left panel. Color coding in all figures, unless otherwise noted:  $\alpha 1$ , dark gray;  $\alpha 2$ , gray;  $\beta$ , black;  $\beta'$ , light gray;  $\beta'$  clamp, violet;  $\epsilon$ , lime green;  $\delta$ , slate blue; HelD, red. b, Comparison to an E. coli EC (PDB ID 6ALH), illustrating dramatic widening of the main channel in RNAP- $\delta$ -HelD.  $\omega$ , cyan; template (t) DNA, brown; non-template

(nt) DNA, beige; RNA, gold. c, Comparison to an *E. coli* GreB-modified EC (PDB ID 6RIN), illustrating similar secondary channel invasion by coiled-coil elements in GreB and HelD.



**Figure 2**

$\epsilon$  subunit. Comparison of the *B. subtilis* RNAP  $\epsilon$  subunit to small domains in subunits D of archaeal RNAP, Rpb3 of eukaryotic RNAP II and AC40 of eukaryotic RNAP I/III.  $\alpha 1$ ,  $\alpha 2$ ,  $\beta$ ,  $\beta'$  subunits and their homologs are colored yellow, gray, black and white, respectively;  $\epsilon$  subunit, lime; HelD, red; subunits specific to archaeal and eukaryotic RNAPs, dark salmon. Dashed circle, cavity in *B. subtilis* RNAP, but not the *E. coli* enzyme, that could accommodate an equivalent of the archaeal subunit N (Rpb10 in RNAP I, II and III). The illustration was prepared using structures with PDB IDs 3HKZ, 6ALH, 6GMH, 4C2M and 6TUT.

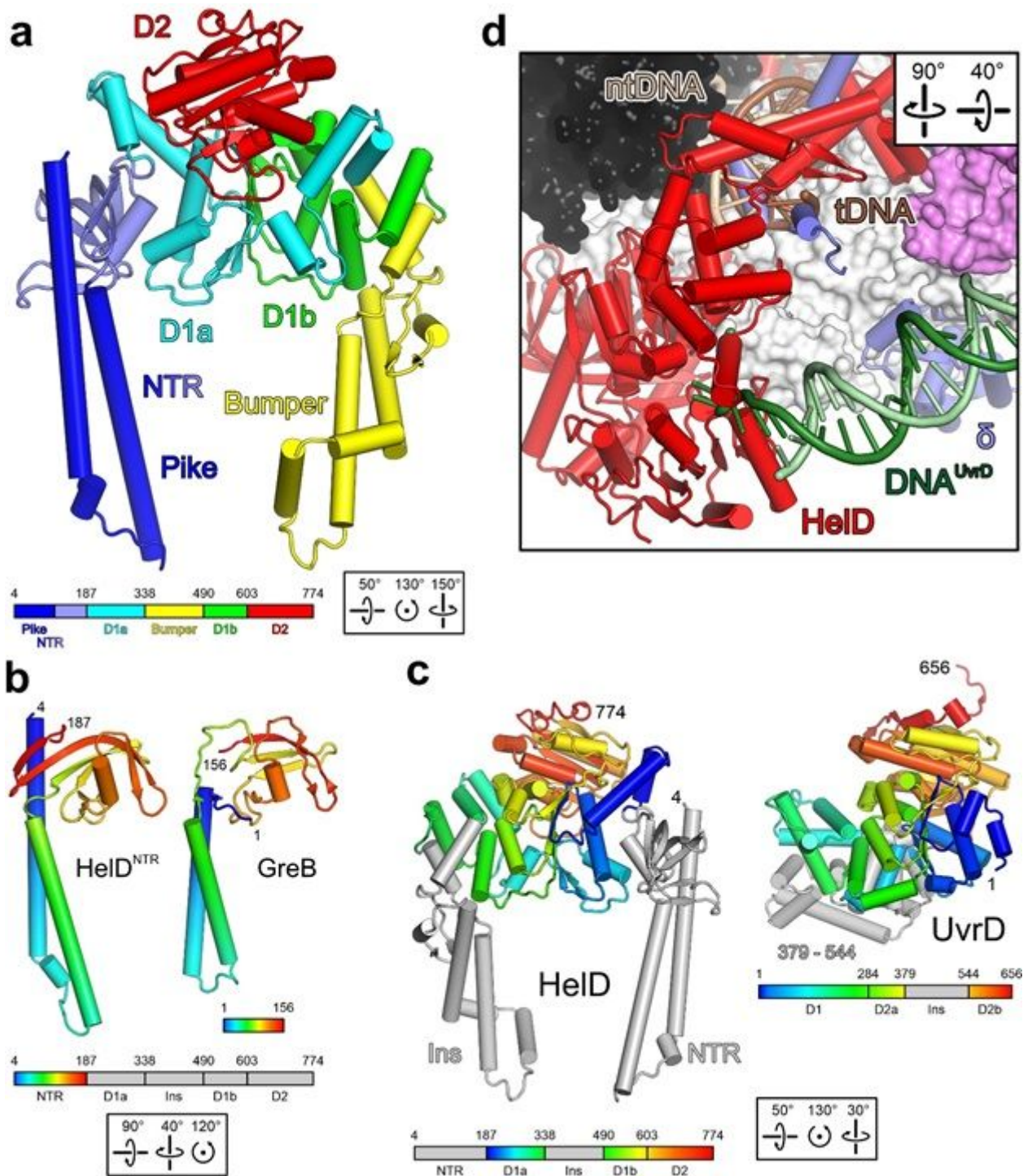


**Figure 3**

HelD architecture. **a**, Cartoon plot of HelD colored by domains (for color-coding see legend). Numbers refer to domain borders. **b**, Comparison of HelD<sup>NTR</sup> to GreB (PDB ID 6RIN) reveals similar topology of the coiled-coils, which insert into the secondary channel, and the globular domains; in GreB, the latter is responsible for high-affinity binding to the RNAP  $\beta'$  rim helices. HelD<sup>NTR</sup> and GreB are rainbow-colored (blue, N-termini; red, C-termini) as indicated in the legend. Numbers refer to domain borders. **c**, Comparison of NTPase domains in HelD and in *E. coli* UvrD (PDB ID 2IS6). The D1-D2 regions are rainbow-colored (blue, N-termini; red, C-termini) as indicated in the legends. Neighboring and inserted

regions (Ins), gray. Numbers refer to domain borders. d, UvrD-bound DNA (dark and light green; PDB ID 2IS6) and nucleic acid scaffold from the *E. coli* EC (PDB ID 6ALH) transferred onto the RNAP- $\delta$ -HeID complex by superpositioning of the UvrD NTPase domains on HeID and of the  $\beta$  subunits, respectively.

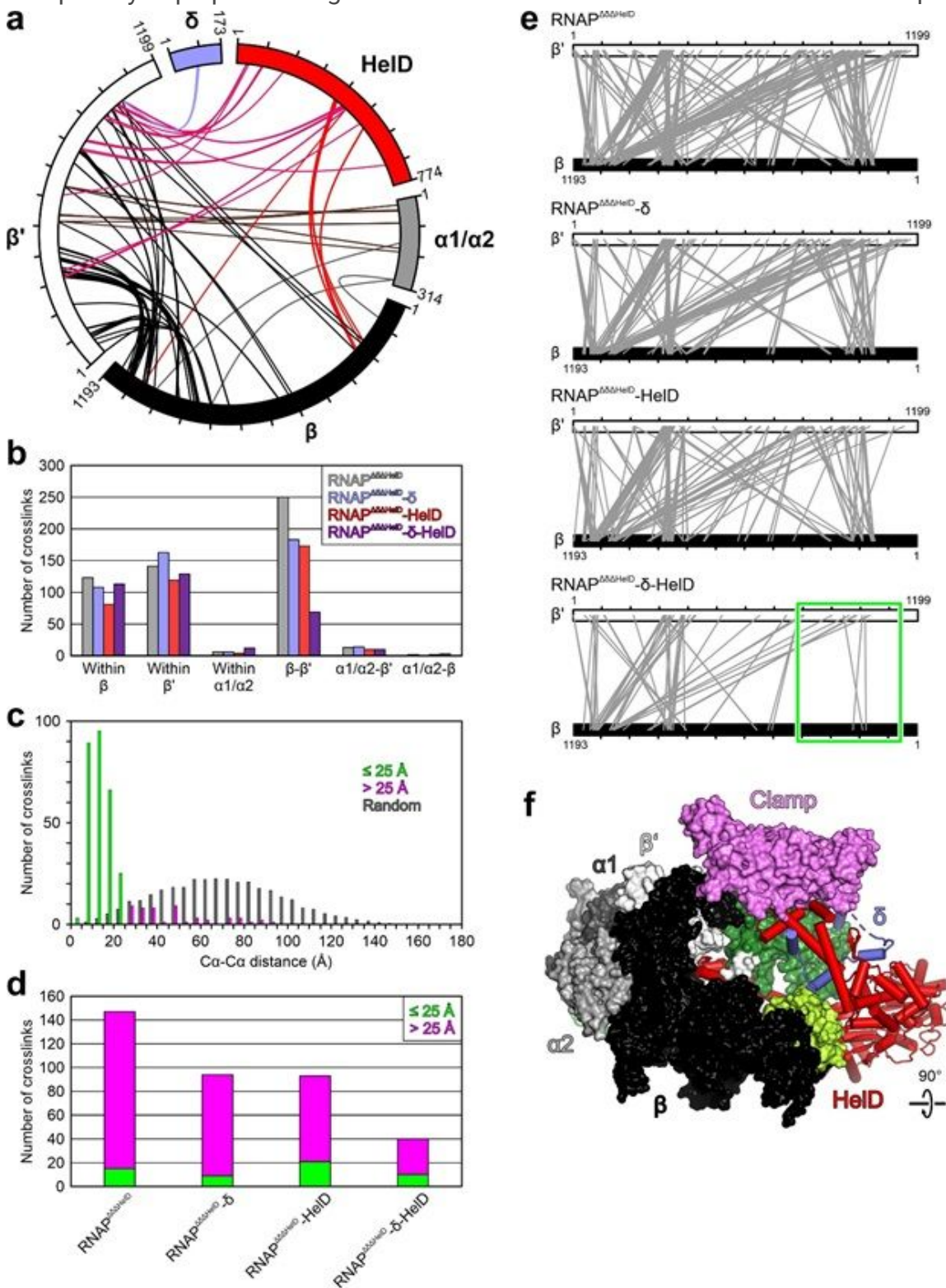
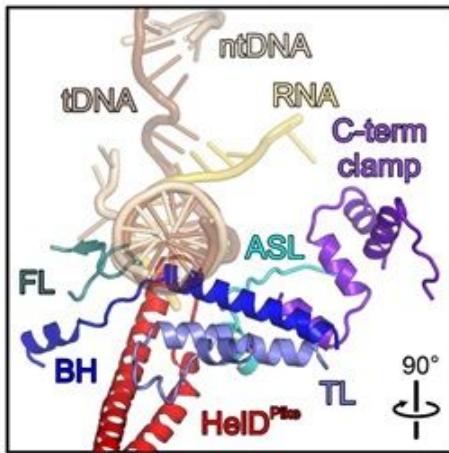


**Figure 4**

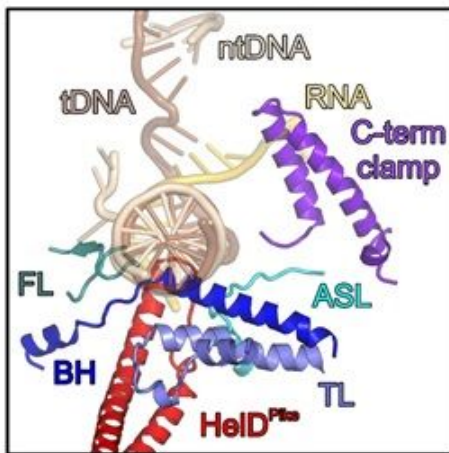
Structure probing by CLMS. a, Map of hetero-protein crosslinks observed in RNAP $\Delta\delta\Delta$ HeID- $\delta$ -HeID complex. b, Crosslinks identified in RNAP $\Delta\delta\Delta$ HeID, RNAP $\Delta\delta\Delta$ HeID- $\delta$ , RNAP $\Delta\delta\Delta$ HeID-HeID and

RNAP $\Delta\delta\Delta$ HelD- $\delta$ -HelD. Binding of both  $\delta$  and HelD leads to strongly reduced crosslinking between  $\beta$  and  $\beta'$ . c, Distribution of Ca-Ca distances between crosslinked residue pairs in reference to the RNAP- $\delta$ -HelD structure. Crosslinks with Ca-Ca distances within 25 Å, the theoretical crosslinking limit of sulfo-SDA, green; crosslinks with Ca-Ca distances > 25 Å, magenta; distance distribution of random residue pairs in the RNAP- $\delta$ -HelD structure, gray. d, Crosslinks between  $\beta$  and  $\beta'$  identified from the four crosslinked complexes. Crosslinks are color-coded as in (b). In the RNAP $\Delta\delta\Delta$ HelD- $\delta$ -HelD complex, a significantly reduced number of  $\beta$ - $\beta'$  over-length crosslinks (in reference to the RNAP- $\delta$ -HelD structure) compared to the RNAP $\Delta\delta\Delta$ HelD, RNAP $\Delta\delta\Delta$ HelD- $\delta$  and RNAP $\Delta\delta\Delta$ HelD-HelD complexes suggests that  $\delta$  and HelD cooperate to stabilize an open conformation of RNAP. e, Comparison of  $\beta$ - $\beta'$  crosslinks observed with RNAP $\Delta\delta\Delta$ HelD, RNAP $\Delta\delta\Delta$ HelD- $\delta$ , RNAP $\Delta\delta\Delta$ HelD-HelD and RNAP $\Delta\delta\Delta$ HelD- $\delta$ -HelD. Green boxed region, crosslinks between the  $\beta_{1/2}$  lobes (residues 146-248) and the  $\beta'$  shelf and jaw (residues 794-1141) observed in the first three complexes but almost absent in RNAP $\Delta\delta\Delta$ HelD- $\delta$ -HelD. f, Structure of the RNAP- $\delta$ -HelD complex highlighting the  $\beta_{1/2}$  lobes (residues 146-248; lemon green) and  $\beta'$  shelf and jaw (residues 794-1141; forest green), which largely lack crosslinks in the presence of  $\delta$  and HelD (green box in e).

**a** Monomeric RNAP- $\delta$ -HeID



**b** Dimeric RNAP- $\delta$ -HeID



**c** *E. coli* EC

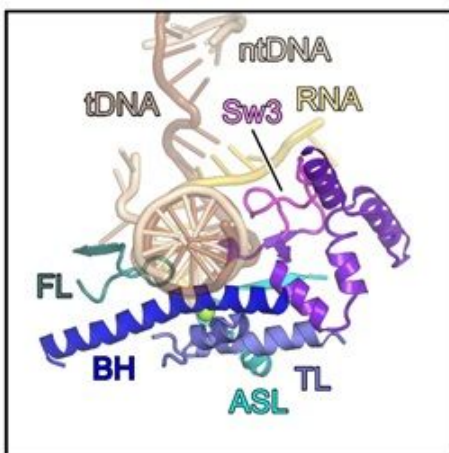


**Figure 5**

Active site dismantling. a, b, RNAP active site environments in monomeric RNAP- $\delta$ -HeID (a) and dimeric (b) RNAP- $\delta$ -HeID, showing HeID-mediated active site dismantling. Comparison to (Newing et al., submitted) suggests that the presence of  $\delta$  promotes more severe active site penetration by HeIDPike. Nucleic acids of an *E. coli* EC (PDB ID 6ALH) were transferred to RNAP- $\delta$ -HeID by superposition of the  $\beta$  subunits.  $\beta$  elements: FL (fork loop), teal; C-term clamp (C-terminal clamp), purple; Sw3, magenta.  $\beta'$

elements: ASL, cyan; BH (bridge helix), blue; TL (trigger loop), slate blue. The catalytic Mg<sup>2+</sup> ion (green sphere) is lost from RNAP- $\delta$ -HelD upon HelDPike invasion. c, Comparison to the RNAP active site environment in an *E. coli* EC (PDB ID 6ALH).

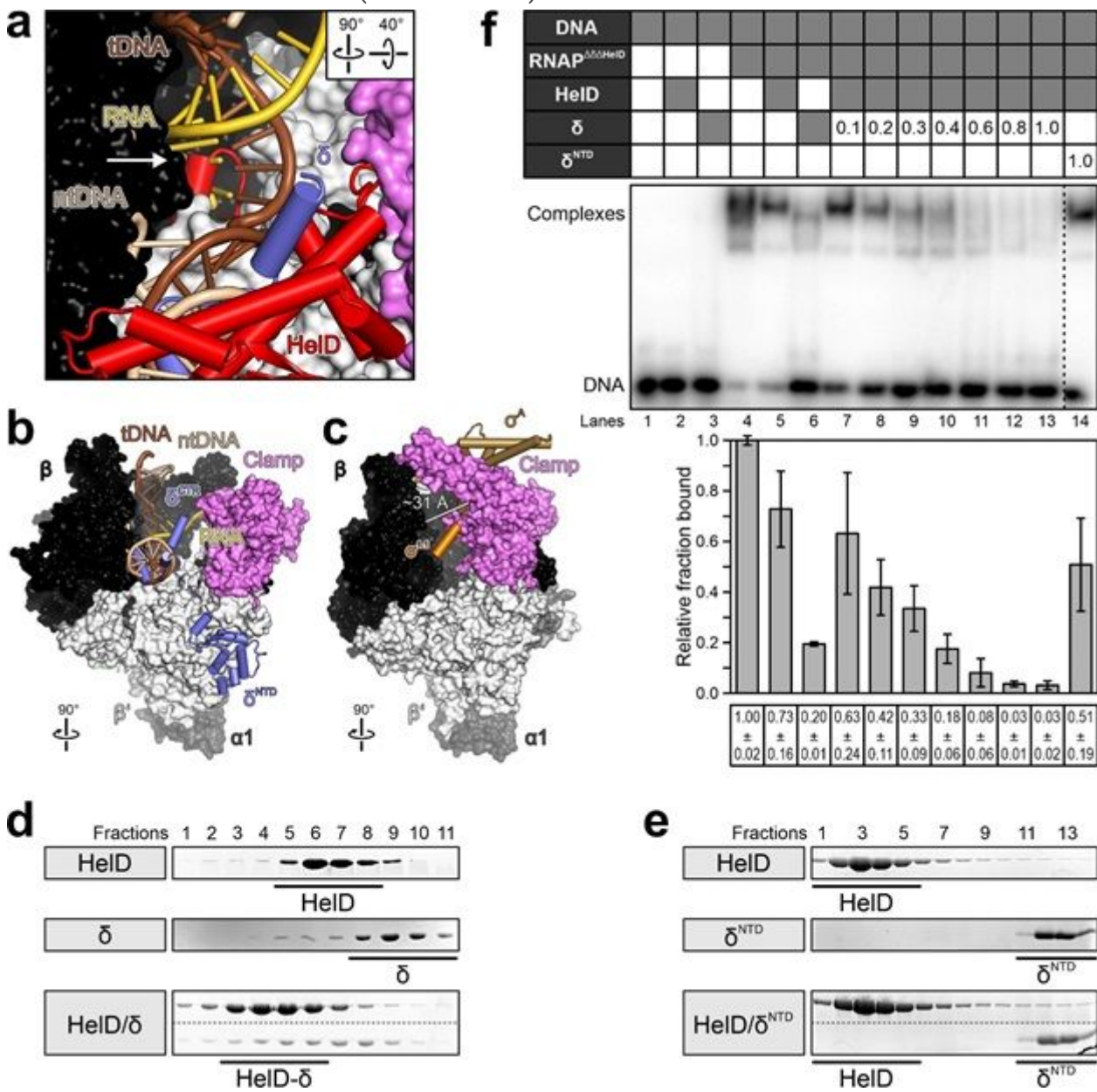


**Figure 6**

HelD/ $\delta$ -mediated RNAP recycling. a, Close-up view of RNAP active site region in RNAP- $\delta$ -HelD, with a nucleic acid scaffold from the *E. coli* EC (PDB ID 6ALH) transferred onto the RNAP- $\delta$ -HelD complex by superpositioning of the  $\beta$  subunits, illustrating direct competition of the HelDNTR coiled-coil tip with RNA (white arrow). b, Nucleic acid scaffold from the *E. coli* EC (PDB ID 6ALH) transferred onto the RNAP- $\delta$ -HelD complex (HelD omitted) by superpositioning of the  $\beta$  subunits, showing competition of  $\delta$ CTR with the downstream DNA duplex in the main channel. c, Comparison to an *M. smegmatis*  $\sigma$ A holoenzyme structure (PDB ID 6EYD), showing analogous positioning of  $\delta$ CTR and the  $\sigma$ 1.1 region in the main channel and the reduced channel width in the  $\sigma$ A holoenzyme.  $\sigma$ A, sand-colored;  $\sigma$ 1.1, orange. d, e, SDS-

PAGE monitoring SEC of a HeID/ $\delta$  mixture (d, lower panel), compared to a HeID/ $\delta$ NTD mixture (e, lower panel), compared to SEC runs of the isolated proteins (upper two panels). Analyzed fractions (numbers above the gels) were identical for the groups of three runs but different fractions were analyzed in (d) and (e). f, EMSA monitoring binding of DNA to various RNAP complexes. Top panel, samples analyzed; gray boxes, respective component added (proteins in equimolar amounts to RNAP $\Delta\delta\Delta$ HeID). Numbers, molar ratios of  $\delta$  or  $\delta$ NTD relative to RNAP $\Delta\delta\Delta$ HeID added. Middle panel, native PAGE analysis. All lanes are from the same gel, some lanes removed for display purposes (dashed line). Bottom panel, quantification of the data shown in the middle panel. Values represent means of DNA bound relative to RNAP $\Delta\delta\Delta$ HeID alone  $\pm$  SD for three independent experiments.

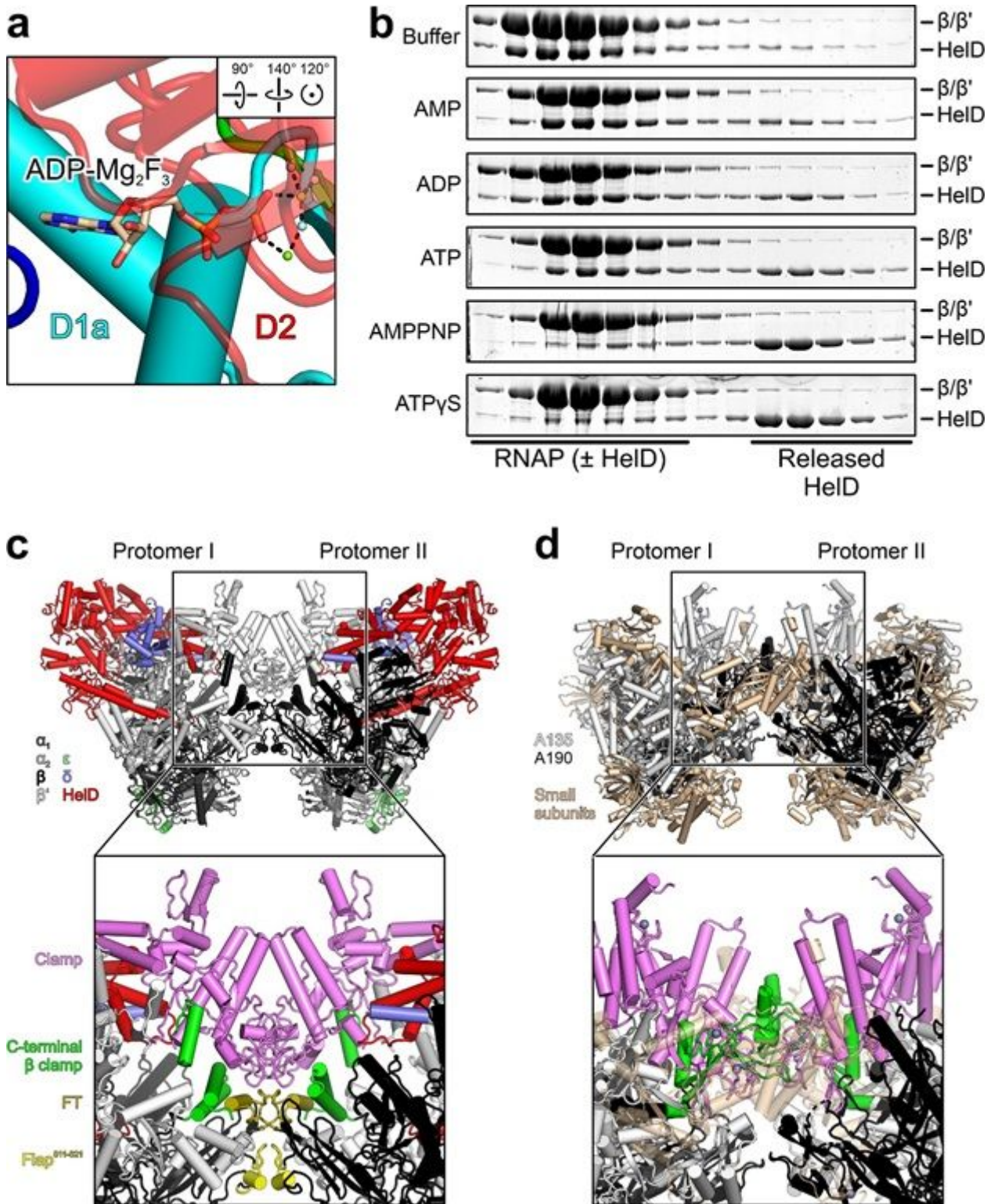


**Figure 7**

HelD release and RNAP-HelD complex dimerization. a, Close-up view of the ATP binding site of HelD, with ADP-Mg<sub>2</sub>F<sub>3</sub> from a UvrD complex (PDB ID 2IS6) transferred by superpositioning of the UvrD NTPase domains on HelD, illustrating clashes with the nucleotide. ADP-Mg<sub>2</sub>F<sub>3</sub> shown as sticks and colored by atom type; carbon, beige; nitrogen, blue, oxygen, red, phosphorus, orange; magnesium ions, green; fluoride ions, light blue. b, SDS-PAGE analysis of SEC runs after treating RNAP-δ-HelD with buffer or the

nucleotides indicated on the left. For full gels, see Extended Data Fig. 6b. c, Structure of dimeric RNAP- $\delta$ -HelD. Inset, close-up view on the dimer interface. The two protomers interact via the elements highlighted in colors;  $\beta'$  clamp, violet; C-terminal  $\beta$  clamp, green;  $\beta$  flap tip (FT), olive; residue 811-821 of the  $\beta$  flap (Flap811-821), yellow. d, Structure of a hibernating RNAP I dimer (PDB ID 4C2M). A135 subunit, black; A190 subunit, white; small subunits, beige. Inset, close-up view on the dimer interface. A190 clamp, violet; C-terminal A135 clamp, green. Model for energy-status-dependent, HelD-mediated RNAP recycling and hibernation. 1°/2°, main/secondary channels; RE, RNA exit tunnel; A/G, general elongation factors NusA/NusG. NusG binds across the active center cleft, while NusA binds to the  $\beta$  FT. Semitransparent icons with dashed lines indicate that the respective factor may be released at the respective step. If the factors remain after termination, NusG will likely be displaced by HelD-induced main channel opening, while the NusA binding site is sequestered in hibernating RNAP-HelD. HelD release and RNAP-HelD complex dimerization. a, Close-up view of the ATP binding site of HelD, with ADP-Mg2F3 from a UvrD complex (PDB ID 2IS6) transferred by superpositioning of the UvrD NTPase domains on HelD, illustrating clashes with the nucleotide. ADP-Mg2F3 shown as sticks and colored by atom type; carbon, beige; nitrogen, blue, oxygen, red, phosphorus, orange; magnesium ions, green; fluoride ions, light blue. b, SDS-PAGE analysis of SEC runs after treating RNAP- $\delta$ -HelD with buffer or the nucleotides indicated on the left. For full gels, see Extended Data Fig. 6b. c, Structure of dimeric RNAP- $\delta$ -HelD. Inset, close-up view on the dimer interface. The two protomers interact via the elements highlighted in colors;  $\beta'$  clamp, violet; C-terminal  $\beta$  clamp, green;  $\beta$  flap tip (FT), olive; residue 811-821 of the  $\beta$  flap (Flap811-821), yellow. d, Structure of a hibernating RNAP I dimer (PDB ID 4C2M). A135 subunit, black; A190 subunit, white; small subunits, beige. Inset, close-up view on the dimer interface. A190 clamp, violet; C-terminal A135 clamp, green.

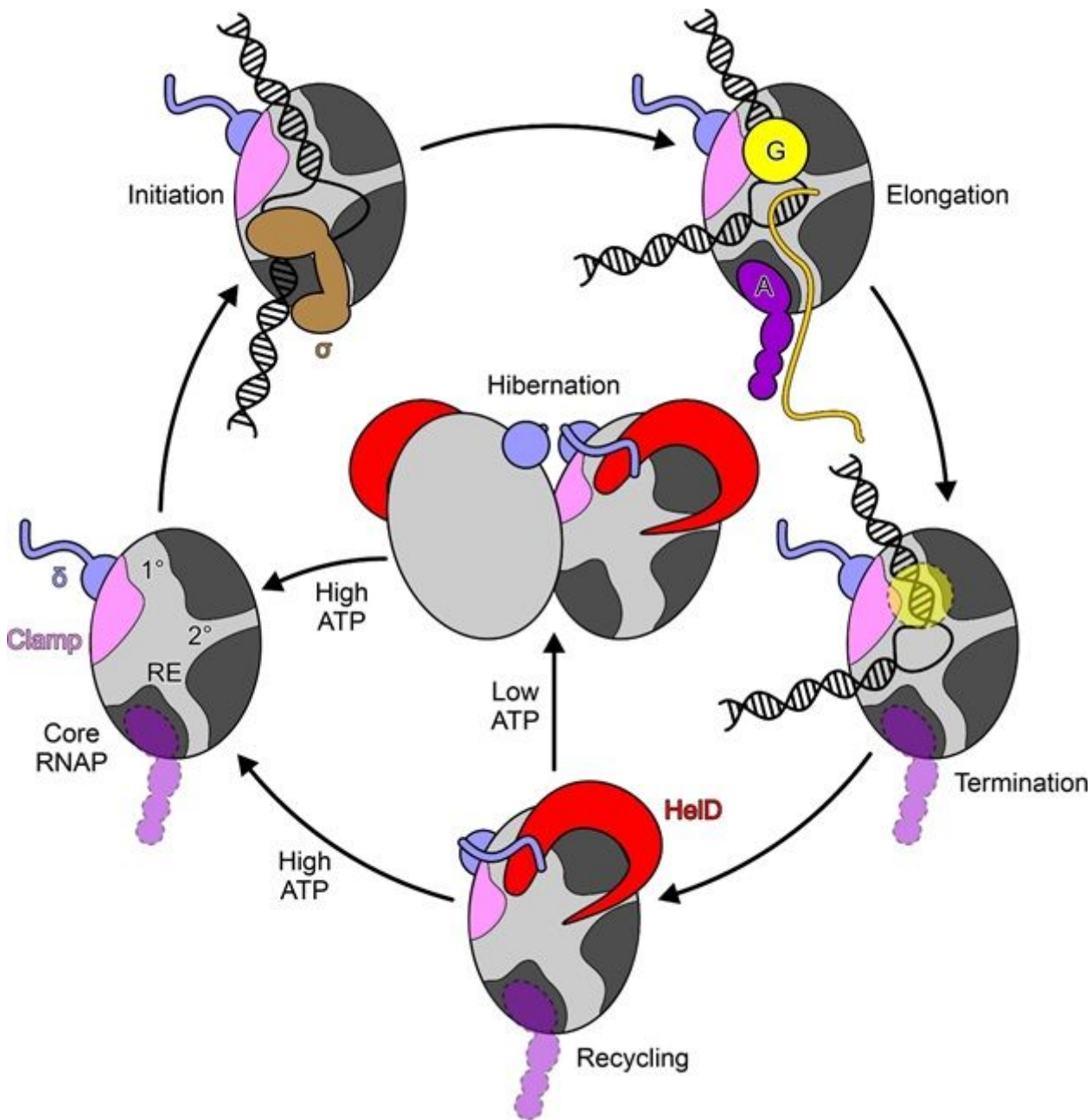


**Figure 8**

Model for energy-status-dependent, HelD-mediated RNAP recycling and hibernation. 1°/2°, main/secondary channels; RE, RNA exit tunnel; A/G, general elongation factors NusA/NusG. NusG binds across the active center cleft, while NusA binds to the  $\beta$  FT. Semitransparent icons with dashed lines indicate that the respective factor may be released at the respective step. If the factors remain after termination, NusG will likely be displaced by HelD-induced main channel opening, while the NusA binding site is sequestered in hibernating RNAP-HelD.

## Supplementary Files

This is a list of supplementary files associated with this preprint. [Click to download.](#)

- [Supplementaryinformation.pdf](#)
- [SupplementaryTable1.pdf](#)